CREATION OF WHITE DWARF PHOTOSPHERIC CONDITIONS IN THE LAB USING THE Z PULSED POWER FACILITY SPRING 2012

JENNIFER ELLIS
ADVISORS: DR. DON WINGET AND DR. ROGER BENGTSON
UNIVERSITY OF TEXAS AT AUSTIN

Abstract. Astronomers routinely determine the masses of white dwarf stars through fitting the observed spectrum to the output from a theoretical atmospheric model, that is dominated by the shapes of the lines. However, when this method is applied to low effective temperature white dwarfs the resulting masses increase dramatically in an unphysical way. In the temperature and density regimes of these low temperature white dwarfs ($N_e > 10^{16}cm^{-3}, T \approx 10,000K$) the line shapes are dominated by Stark broadening. The Stark effect is the shifting of atomic energy levels due to an external electric field, and Stark broadening arises when summing this effect over the electric fields in a plasma. However there are multiple, competing line broadening theories and little laboratory data at the relevant plasma conditions. We are using the x-rays produced by the Z Pulsed Power Facility at Sandia National Laboratories to heat a macroscopic sample of hydrogen gas to white dwarf photospheric conditions, where we then take time-resolved emission or absorption spectra. We have demonstrated that we achieve a plasma at the desired temperatures and electron densities, that is stable for about 100ns. We have also verified our understanding of the heating mechanism driving the plasma conditions. Finally we compare three line broadening theories, those of Vidal-Cooper-Smith [21], Kepple-Griem [22], and Tremblay-Bergeron [20], with each other and to the Z data.

1. Introduction 3
2. Background 7
2.1. The Stark Shift and Stark Broadening 7
2.2. Review of Past Experiments 10
3. Experimental Setup 12
3.1. Z Pulsed Power Facility 12
3.2. The White Dwarf Platform 13
3.3. Validation of Platform 16
4. Results 26
4.1. Comparison of Line Broadening Theories 26
4.2. Comparison of Z Data with Theory 26
5. Conclusions 31
6. Future Plans 32
7. Acknowledgements 33
References 33
8. Appendix I - Balmer line profiles. 35
9. Appendix II - Shot Archive 38

Table of Contents

1. Introduction

White dwarfs are the evolutionary endpoint for approximately 97% of all stars, including one day our Sun. White dwarfs typically contain about 0.6 of the mass of the sun (M_{Sun}) in a volume about the size of the Earth; it was not until the advent of quantum mechanics that it was understood how an object so dense could be supported against gravity.

When most stars run out of hydrogen in their core they begin to fuse helium. It is the energy produced by the fusion reactions inside a star that provides the counterbalance to gravity in order to hold the star up. Helium fusion reactions produce more energy than their hydrogen counterparts, and hydrogen is still burning in a shell around the core, so the radiation pressure is greatly increased and causes the star to inflate into a red giant (increasing in radius as many as 200 times). After moving off the red giant branch stars lose much of their mass in a complicated process that is not well understood. As a star runs out of fusible material in its core it loses that thermal support and begins to collapse due to gravity. The star will continue to collapse until densities are such that a purely quantum mechanical pressure, known as electron degeneracy pressure, begins to support the star against gravity.

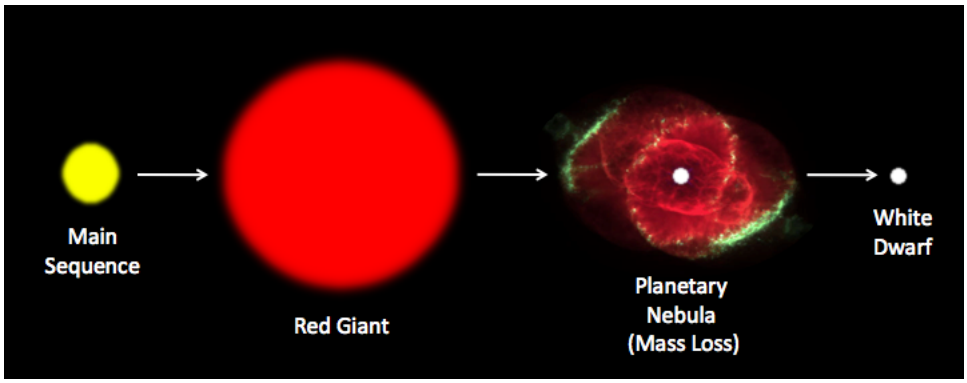

Figure 1. Basic stellar evolution from a main sequence star, like the Sun, to a white dwarf (not to scale).

The Pauli Exclusion Principle is the quantum mechanical principle that no two fermions can be in the exact same quantum state. If electrons are squeezed into the same spatial state they are required to be in different energy states, so compressing more electrons into a volume forces them to have more energy. In white dwarfs, this results in high velocity electrons, which provide the outward pressure that halts the gravitational collapse. This phenomena can also be understood through the Heisenberg uncertainty principle, $\Delta x \Delta p \leq \frac{\hbar}{2}$, where Δx is the uncertainty in position, Δp is the uncertainty in momentum, and $\hbar$ is the reduced Planck's constant. As electrons are compressed Δx decreases, so Δp must increase, leading to high velocity electrons that contribute to the outward degeneracy pressure.

Because white dwarfs are the leftover interiors of stars, and are no longer producing energy through fusion reactions, they are born very hot and spend the rest of their lives cooling off. Their high densities and high surface gravities cause a settling of the heavier elements in the outer layers of the star, leaving an extremely pure outer shell of the lightest element present in the star, be that hydrogen, helium, or even carbon (figure 2). In many ways as a star evolves into a white dwarf it sheds much of its complexity, and therefore becomes an ideal stellar laboratory to study many different physical and astrophysical phenomena, including crystallization, degenerate states of matter, and to place limits on the age of the Galaxy.

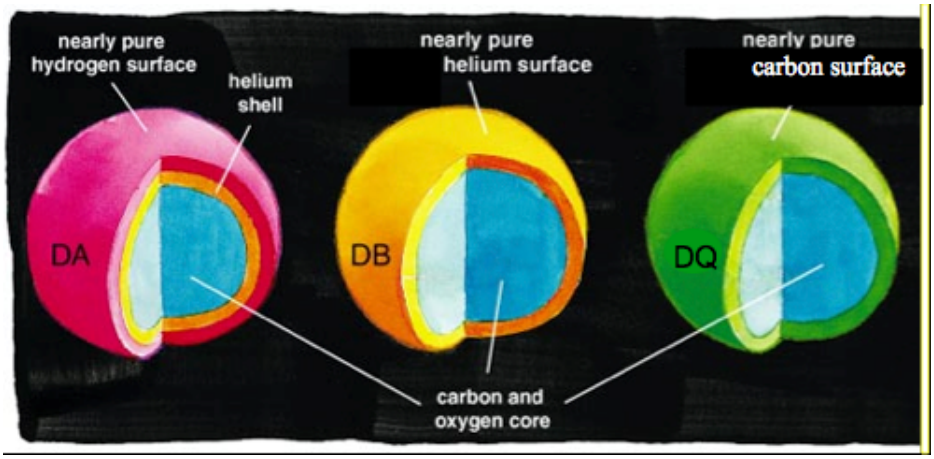

FIGURE 2. White dwarf internal structure (layer thickness not to scale) [1].

However, all of the science that can be done with white dwarf stars is limited by the accuracy in the measurement of the boundary conditions, or the stellar properties of the white dwarfs being observed (namely temperature and mass). Fits of observed white dwarf spectra to atmospheric models are used to determine the photospheric plasma conditions of individual white dwarf stars, and from there global parameters (such as mass) are determined. Spectral fits are used for all stars, but white dwarfs have a problem, as compared to other stars, because they have atmospheres that are 10,000 times denser than main sequence stars, like the Sun, and therefore their absorption lines are very broad.

The spectral lines of a white dwarf are broad primarily due to a phenomenon known as the Stark effect. Generally an atom, such as hydrogen, emits (and absorbs) light at specific wavelengths determined by the allowed energy levels of the atom. However, when an atom is placed in an external electric field those allowed energy levels are shifted in a way that is dependent upon the strength of the field. This shift in the energy levels results in a shift of the wavelength of light that will be emitted or absorbed. Since most white dwarfs are hot a substantial fraction of the atoms in the atmosphere of the star are ionized, and these ions and free electrons will produce local electric fields. Furthermore, since a white

dwarf is dense these ions and free electrons are close enough to the neutral emitters for them to feel a substantial electric field, and hence experience a substantial shift. Summing over a particle distribution in a plasma results in a net broadening effect, referred to as Stark broadening, since some emitters will be in strong local fields and some will not. Therefore comparison of the measured spectra to that of theoretical spectra can be used to obtain stellar parameters, particularly electron density. It should be noted that the higher the atomic energy level the more weakly bound the electron is, and therefore it is more sensitive to the perturbing electric field, making this effect more pronounced in higher order transitions.

However, when this method is applied to large surveys of white dwarf stars a trend emerges, known as the white dwarf upturn, where the measured mass of white dwarf stars increases dramatically with decreasing temperature (figure 3). Utilization of gravitational redshift measurements, which are model independent, to find the average white dwarf mass (figure 4) not only do not show this temperature dependence in the mass determination, but also find a lower average white dwarf mass than obtained by spectroscopic methods [3]. Because

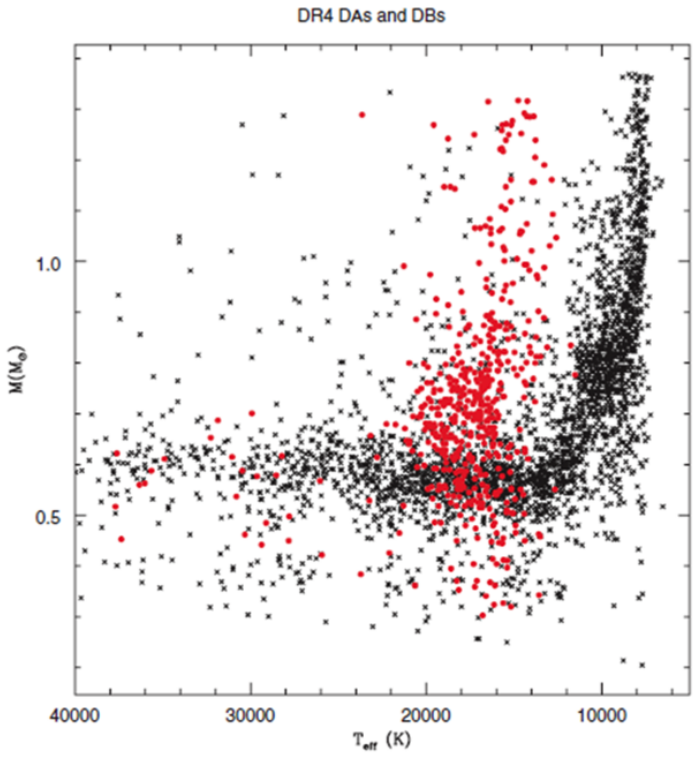

FIGURE 3. Spectrally obtained white dwarf mass as a function of effective temperature. Black: Hydrogen WDs (DA), Red: Helium WDs (DB) [2].

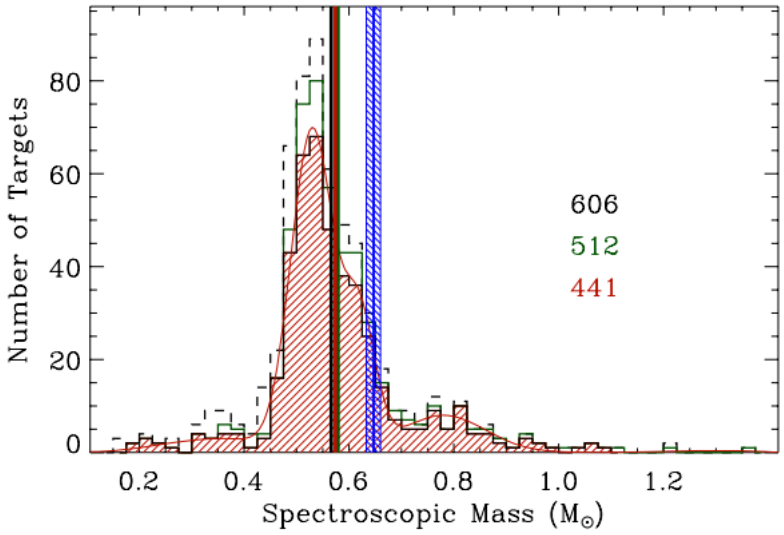

FIGURE 4. Histogram of spectroscopically obtained mass distribution. Also marked is the average spectroscopic mass (orange vertical bar) and the average mass from the gravitational redshift method (blue vertical bar) [3].

white dwarfs are dense, emitted photons have to climb out of a considerable potential well to escape; in doing so they lose energy and therefore are redshifted, the size of this redshift is dependent only upon the mass of the white dwarf. However any given white dwarf will have some random velocity through space, relative to that of Earth, and therefore it is impossible to disentangle the gravitational redshift from the Doppler shift, so this method cannot be used to obtain masses of individual stars. Though if the velocity distribution is random, then averaging over a large sample of white dwarfs will cancel out the Doppler component, leaving only the gravitational redshift, allowing for the determination of an average white dwarf mass.

Because this upturn is not seen when spectrally independent methods are utilized and the evolution of white dwarf stars is simply a cooling sequence, it is not believed that this trend is physical.

Stark broadening is the largest contribution to the width of white dwarf spectral lines. There exist several competing line broadening theories and almost no laboratory data in the relevant temperature and density regimes ($T \approx 11,000K, N_e > 10^{16} cm^{-3}$, see figure 5). Therefore, in collaboration with Sandia National Laboratories, we use the Z Pulsed Power Facility to produce white dwarf photospheric conditions in the laboratory, for the direct measurement of spectra in these regimes. This will allow us to benchmark the various theories, which can then lead to an improvement of the atmospheric models and a more accurate determination of white dwarf mass.

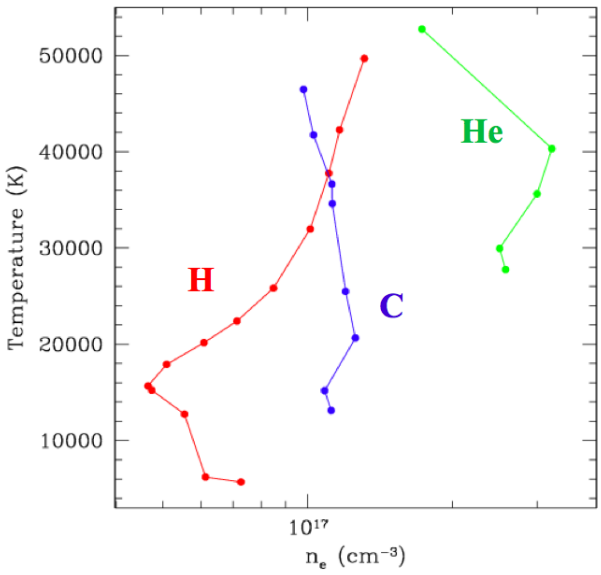

FIGURE 5. Effective temperature and electron densities of hydrogen, helium, and carbon white dwarfs (log g = 8) [4].

2. BACKGROUND

2.1. **The Stark Shift and Stark Broadening.**

The first step in understanding hydrogen line broadening under these conditions is understanding the Stark effect for a hydrogen atom in an external electric field, $\vec{E} = E\hat{z}$. The Hamiltonian for this system is

$$H = -\frac{\hbar^2\vec{\nabla}^2}{2m} - \frac{e^2}{4\pi\epsilon_0 r} + eEz = H_0 + H'$$

where H_0 is the unperturbed Hamiltonian for the hydrogen atom, and H' is the perturbative interaction of the electron with the electric field. Solving the Schrödinger equation for the unperturbed hydrogen atom gives

$$H_0|\psi^0_{nlm}\rangle = E^0_n|\psi^0_{nlm}\rangle$$

$$\psi^0_{nlm} = R_{nl}(r)Y_{lm}(\theta,\phi)$$

$$E^0_n = -\frac{e^2}{8\pi\epsilon_0 n^2} = \frac{-13.6eV}{n^2}$$

The unperturbed energy levels are degenerate, in that in a given level n there are $n-1$ allowed l values, and for a given l there are $2l+1$ allowed m values. Therefore degenerate perturbation theory [5] must be applied in order to find the new energy levels of the

perturbed hydrogen atom. To first order the new energies will be $E = E^0 + E^1$ where E^1 is given by the eigenvalues of the perturbation matrix,

$$H'_{jk} = \langle \psi^0_j | H' | \psi^0_k \rangle = eE \langle \psi^0_j | z | \psi^0_k \rangle$$

The matrix element connecting any two states of the hydrogen atom is

$$\langle \psi^0_{(nlm)_j} | z | \psi^0_{(nlm)_k} \rangle = \int \psi^{0*}_{(nlm)_j} z \psi^0_{(nlm)_k} d^3r$$

$$= \int R_{(nl)_j}(r) Y^*_{(lm)_j}(\theta, \phi)(r\cos\theta) R_{(nl)_k}(r) Y_{(lm)_k}(\theta, \phi) r^2 \sin\theta dr d\theta d\phi$$

$$= \int R_{(nl)_j}(r) R_{(nl)_k}(r) r^3 dr \int Y^*_{(lm)_j}(\theta, \phi) Y_{(lm)_k}(\theta, \phi) \cos\theta \sin\theta d\theta d\phi$$

Because the angular portions of the wave functions, $Y_{lm}(\theta, \phi)$, are given by spherical harmonics the angular portion of the above integral is zero unless $m_j = m_k$ and $l_j = l_k + 1$ or $l_k - 1$. This greatly simplifies the perturbation matrix H'_{jk} since most of the elements will be zero. To actually calculate the Stark shift for any given unperturbed energy level n all that remains is to evaluate the radial portion of the above integral, for the non-vanishing matrix elements.

As an example, the $n = 2$ level of the hydrogen atom (which is the energy level associated with the Balmer transitions) has four degenerate levels: $\psi_{200}, \psi_{210}, \psi_{211}$, and ψ_{21-1}. Therefore we can construct H'_{jk} in the ordered basis $\{|\psi^0_{200}\rangle, |\psi^0_{210}\rangle, |\psi^0_{211}\rangle, |\psi^0_{21-1}\rangle\}$. However, due to the angular selection rules above, there will only be two nonzero elements:

$$H' = \begin{bmatrix} 0 & H & 0 & 0 \\ H & 0 & 0 & 0 \\ 0 & 0 & 0 & 0 \\ 0 & 0 & 0 & 0 \end{bmatrix}$$

Here $H = eE\langle \psi^0_{200} | z | \psi^0_{210} \rangle = -3eEa_0$, where a_0 is the Bohr radius. The eigenvalues of this H' matrix now give the shifted energies to first order, and the eigenvectors are the new shifted wavefunctions to zeroth order.

If the above analysis is applied to the $n = 3$ level of hydrogen you can see first of all that the Stark effect is much stronger in the higher energy level, and second that at high electric fields the $n = 2$ and $n = 3$ levels begin to mix. This leads to a merging of spectral lines and an associated effect known as continuum lowering.

It should be noted that the expressions above were derived under the assumption that the external electric field was a small perturbation compared to the electric field associated with the hydrogen atom. In high electric fields the linear relationship between external field strength and energy shift breaks down, because higher order perturbation theory is needed to accurately describe the situation. Therefore, although the specific expressions derived under the perturbative assumption cannot be extrapolated to higher electric fields the general trends are still relevant. The extreme limit of this occurs approximately when

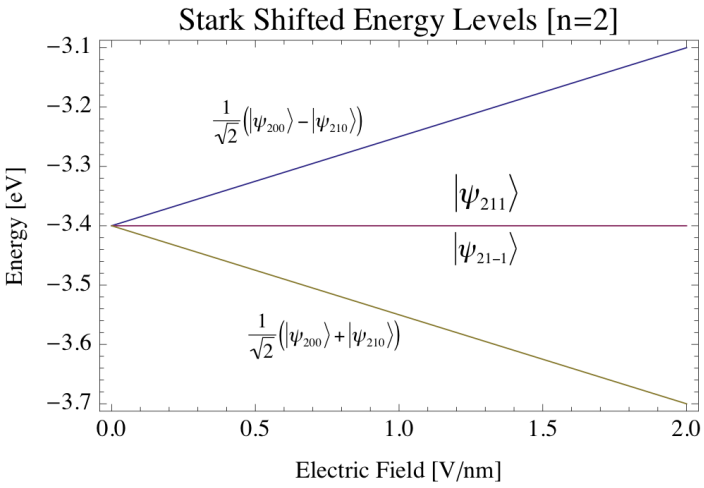

FIGURE 6. Stark shift of the n=2 level of hydrogen as a function of electric field strength.

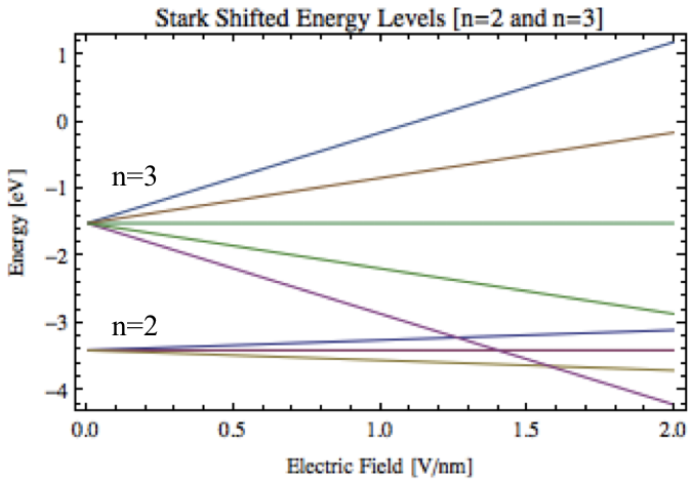

FIGURE 7. Stark shift of the $n = 2$ and $n = 3$ levels of hydrogen as a function of electric field strength.

$e/r_{orbit} \approx e/ < r_{ion} >$ or when $e/a_0 \approx en^{1/3}$, where a_0 is the Bohr radius and n is the electron (or ion) number density, resulting in an electron density of $n \approx 6.7 \times 10^{24}$ cm^{-3}. Additionally, in order to calculate the spectrum from a plasma in these regimes, be it a white dwarf or a gas cell in a laboratory, you no longer have a lone hydrogen atom and must account for the ensemble properties of the plasma in question.

2.2. **Review of Past Experiments.**

The ideal experiment with which to test line broadening theories would utilize a plasma that is both stationary and homogeneous, and would have spectrally independent methods for measuring the plasma parameters, namely temperature and electron density. However, these simultaneous requirements are often at odds and past experiments can be broken down into those that are stationary and those that are homogeneous [6]. While there have been experimental studies spanning orders of magnitude in electron density, I am going to focus on the high density ($N_e > 10^{16} cm^{-3}$) regime, which is applicable to white dwarf atmospheres. For a sample of low density experiments see references [7] through [9].

A large number of the experimental studies of hydrogen broadening in the high density regime have focused on the Balmer Hβ line [10, 11, 12]. Hβ is at a convenient wavelength for observation in the optical, has a characteristic profile (figure 8), and is often optically thin, which has made it the logical and accessible case with which to benchmark line broadening theories, even though it is less sensitive to this broadening than the higher order Balmer lines.

The combined results of many experiments, of both the homogeneous and stationary type, show that theoretical and experimental electron densities for Hβ agree to within about 7% [6]. It is seen across the board that all theoretical profiles over-predict the structure in the line center but overall agreement and half-widths are fairly accurate. It was later found

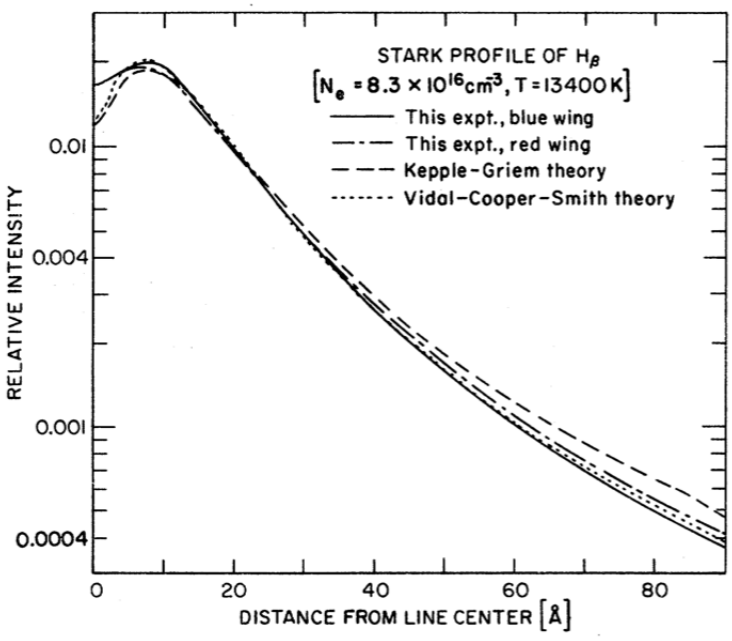

FIGURE 8. Wiese et al. published Hβ profile [17].

that much of the discrepancy in the line core could be corrected if ion motion was taken into account, relaxing the quasistatic approximation in the line core [13, 14].

While there has been experimental vetting of, and subsequent faith placed in, the Hβ profile, the remaining lines in the Balmer series have not been quite so well explored. Hα is optically thick at these densities, so measurements of the Hα profile have been made either in a mixture or in a pure hydrogen gas while accounting for optical depth effects [15]. Comparisons have shown theoretical and experimental agreement to within 10%, which is within the combined experimental and theoretical errors [15]. However, it is the higher order lines that are more of a consideration for white dwarf atmospheric fits.

There have been two main experiments simultaneously measuring profiles of multiple Balmer lines, Hα, Hβ, Hγ, and Hδ [16, 17], which I will discuss further. Hill and Gerardo [16] used a critically damped discharge tube, which provided a spatially uniform plasma column for comparison of the the measured half-widths to theoretical half-widths from Griem et al. Two multiple-pass laser interferometers, in the visible and infrared, were used for a spectrally independent determination of electron density to better than $\pm 2\%$. The reproducibility of the discharge was shown to be very good, and a rapid scanning spectrometer was used. Multiple discharges were measured and combined for each profile. For Hβ, line shape data was taken for electron densities of $(1.3 - 8.5) \times 10^{16}\text{cm}^{-3}$ and it was found that the theoretical profiles were accurate to better than $\pm 3.5\%$ throughout this range. Only two profiles were recorded for Hγ, at electron densities of 1.30×10^{16} and $3.71 \times 10^{16}\text{cm}^{-3}$. The measured H$\gamma$ half-widths were larger than the theoretical prediction for those electron densities by 10.8 and 16.4%. Hδ profiles were also measured, at electron densities of $(1.3 - 2.8) \times 10^{16}\text{cm}^{-3}$, however at the time there were no tabulated theoretical profiles available for Hδ at these densities, and the half-width therefore had to be extrapolated from the tabulated values at $10^{14} - 10^{16}\text{cm}^{-3}$. The experimental half-widths were found to be 7% narrower than expected by the extrapolated theory. You can see that agreement between experiment and theory is good for Hβ, but for the higher order lines that agreement deteriorates, and deteriorates in an inconsistent way.

On the other hand, Wiese, Kelleher, and Paquette [17] used a wall-stabilized arc, providing a stationary but nonuniform plasma, to which they compared the theoretical profiles of Kepple-Griem (KG) and Vidal-Cooper-Smith (VCS). Arcs are radially inhomogeneous but cylindrically symmetric, therefore the Abel inversion process was utilized to deconvolve the spectral contribution from different radii. These different radii then correspond to different electron densities, which were derived from absolute intensity measurements. While profiles were measured for Hδ and compared with KG (no VCS profiles for this line were available at the time) no analysis of the widths of this line was made. They noted that KG over predicts structure in the core of Hδ, and deviates significantly in the wings. For the remaining measured lines (Hα, Hβ, and Hγ) $\frac{1}{2}$, $\frac{1}{4}$, and $\frac{1}{8}$ widths were analyzed, in addition to basic comparison of the line shapes. It was seen that the theoretical electron densities, of both KG and VCS, agreed with the experimentally determined values to within 10% for Hβ, however for Hγ this agreement remains to about 10% for KG but deteriorates to about

20% for the VCS theory. For Hα this deteriorates even further, which is attributed to discrepancies in the line center, which have a large effect on the position of the $\frac{1}{2}$, $\frac{1}{4}$, and $\frac{1}{8}$ widths. Wiese et al also compared the widths of the different lines at the same electron density, as a check of the internal consistency of the theories. They observed differences between the experimental and theoretical ratios of $5-15\%$ for the Hβ/Hγ ratio, and much larger discrepancies for the Hβ/Hα ratio.

While these past experiments have served as a benchmark, especially for Hβ, further experimental evaluation of the Balmer lines in high density plasmas is desirable [6]. Current experimental studies have been restricted to measure only lines as high as Hδ, however the discrepancies between the various line broadening theories are more pronounced for the higher order lines, and data does not exist at these densities. Although, it must be kept in mind that at very high electron densities (above a few times 10^{17} cm^{-3}) these higher order lines begin to become broadened so much, that they merge into the continuum and are no longer observable.

Additionally, more investigation of the internal consistency between lines is needed, and is especially relevant to the determination of stellar properties, where many lines in the Balmer series are fit simultaneously. These investigations have been conducted in the low density regime [7] [8], where they found agreement within the combined theoretical and experimental errors for Hγ – H$_{12}$. At higher electron densities ($2\times10^{16}-2\times10^{17}$ cm^{-3}) Bengtson et al. [18] found that the ratio of electron densities obtained from Hβ to those found from Hγ line profiles was 1.01, using the theory of Kepple-Griem. However, they did not look at Balmer lines higher than Hγ.

3. Experimental Setup

3.1. **Z Pulsed Power Facility.**

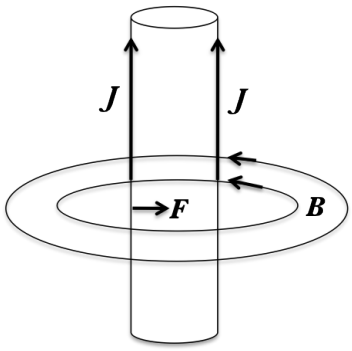

Figure 9. Lorentz force on an axial current density, $\vec{J}$.

The Z Pulsed Power Facility, housed at Sandia National Laboratories in Albuquerque, New Mexico, is currently the most powerful x-ray generator in the world. The Z machine is an application of the Lorentz force, $\vec{F} = \int \vec{J} \times \vec{B}\, dV$. The basic principle behind its operation is that currents running in parallel wires will create an inward force, pulling the wires together (figure 9).

In a Z pinch, such as the Z Machine, enough current is run through a cylinder of wires so that they vaporize to form a plasma that is still conducting. The Lorentz forces now act on the plasma, pinching it inward along the axis. This shock heats the plasma and it emits a pulse of radiation.

The Z Machine runs about 26 million amps of current through a small cylinder of tungsten wires in tens of nanoseconds. This achieves an x-ray output of approximately 2.7 megajoules, with peak x-ray powers of 350 terawatts. While Z has many applications, and is used to study many high energy density phenomena, for our purposes Z is just a big x-ray source, and is the driver that heats our plasma to white dwarf photospheric conditions.

3.2. **The White Dwarf Platform.**

In order to produce a macroscopic plasma at white dwarf photospheric conditions we place an $\approx$ 19 cm^3 steel gas cell (figure 10) 35 cm away from the pinch (figure 11), with a rectangular window 1 cm $\times$ L cm, where L is the axial length of the cell. The window is a 1.5μm thick sheet of Mylar ($C_{10}H_8O_4$), which is initially transparent to much of the X-ray spectrum emitted by the Z-pinch. However, in the case of a hydrogen gas fill, the photons that would interact with the hydrogen gas are absorbed by the Mylar, so the gas inside the cell is also transparent to X-rays from the pinch. Therefore a gold sleeve is inserted into the interior of the gas cell. The gold absorbs the incident radiation, is heated to approximately 5eV, and then reradiates a nearly blackbody spectrum, heating the hydrogen gas to approximately 1eV. On either end of the cell are two large cylindrical ears. These are also filled with gas but are isolated from the radiation emitted by the gold, and are consequently at a lower temperature (the time scale for heat diffusion into the

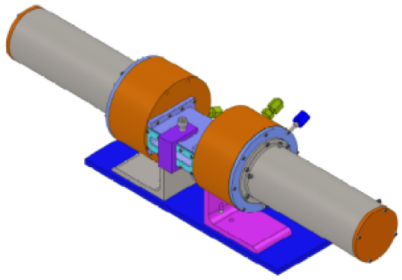

FIGURE 10. Basic gas cell design.

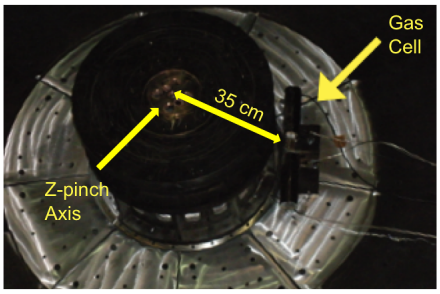

FIGURE 11. Gas cell in place, along line of sight from Z.

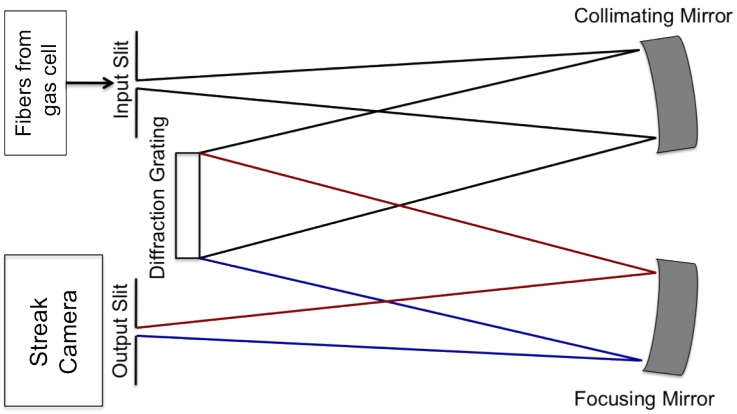

FIGURE 12. Spectrometer design.

ears is slow compared to the duration of the measurement). The ears therefore serve as a buffer region, protecting the optics from the hot plasma. Several different variations of this basic cell design have been implemented, and will be discussed when presenting the relevant data.

On the far side of either ear is a fused silica window (which completes the vacuum) and the option to attach a lens coupled fiber-optic cable. These fiber-optics pipe the signal to a remote location, where they are fed into the streaked visible spectrometer (SVS) system. The fibers couple to a focusing lens, focusing the signal onto the input slit of a 1m Czerny-Turner spectrometer (McPherson, model #2061). We have the option of using several different gratings, but have almost exclusively employed one with 150 grooves/mm, resulting in a spectral resolution of ≈ 8Å.

At the exit slit of the spectrometer is a EG&G streak camera (model #L-CA-24), which gives both wavelength and time resolution, when used in conjunction with a spectrometer. The entrance of a streak camera is a narrow slit and a photocathode. Photons illuminating the entrance slit generate photoelectrons when they hit the photocathode. These electrons are then accelerated through a microchannel plate (MCP) by a constant voltage, which produces many secondary electrons for every original photoelectron, amplifying the signal. Once the electrons leave the MCP a constant parallel voltage, and a time varying (increasing) perpendicular voltage is applied. This accelerates the electrons along their parallel line of flight towards a phosphor, while simultaneously sweeping them in time. Once the electrons hit the phosphor they are converted back into photons, which are then registered on a piece of film (Kodak, TMAX 400) at the output of the streak camera. This allows for the measurement of wavelength dependent intensity over time. This film is developed along with an intensity calibrated piece of film called a step wedge. Once developed, the shot data and the step wedge are both scanned into a digital format where we can then apply the step wedge calibration to our data.

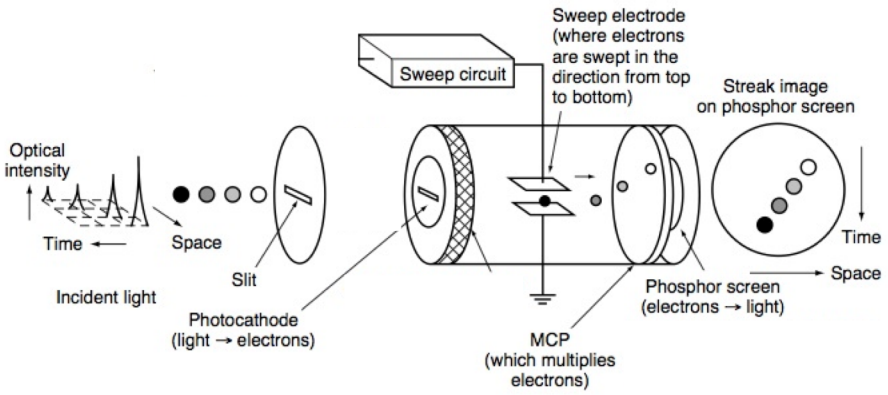

FIGURE 13. Basics of streak camera operation [19].

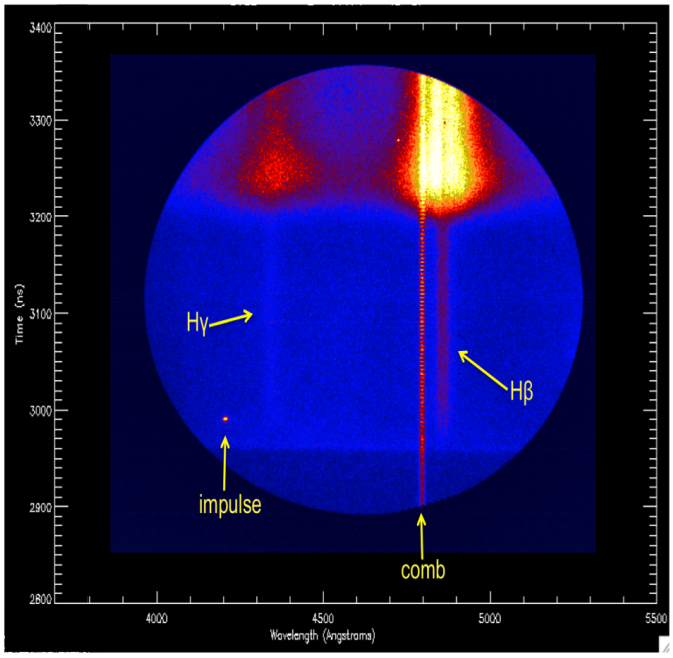

FIGURE 14. Example of reduced data. At the time this data was taken there was no available laser in this spectral region.

We use two different fiducials to keep track of time during the measurement, allowing the conversion of distance along film to time during experiment. The first of these is a pulsed laser of known period, called the comb, which marks time throughout the shot. The second is a one time laser pulse, known as the impulse, which is triggered by a signal from the Z-facility and is used to connect time during our measurement to Z-machine timings. Both of these are lasers are directly coupled to the streak camera input slit, without going through the spectrometer system. We also employ lasers, which are passed through the spectrometer, as wavelength fiducials when we have access to a laser of appropriate wavelength.

3.3. **Validation of Platform.**

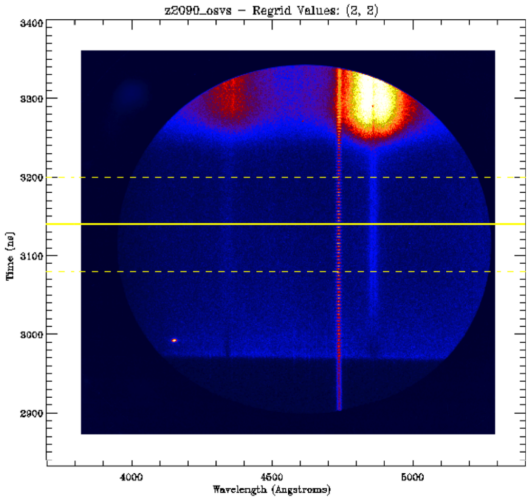

FIGURE 15. z2090 - Steady state period, over which average was taken is marked.

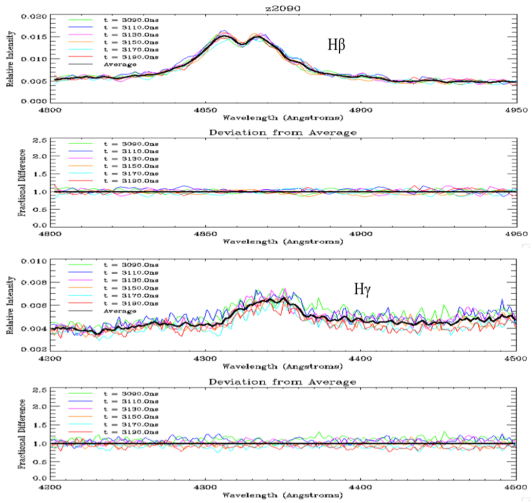

FIGURE 16. 20ns line-outs over the steady state region of z2090 and their average, for Hβ and Hγ.

The first step in this project was to show that we can in fact create a steady state plasma at the relevant conditions, by utilizing the Z-pinch radiation. Comparing narrow (10-20ns) lineouts from the streak data shows that there is in fact a region in time where the hydrogen line shapes are not changing (figure 16) for upwards of 100ns. This stability in the line shapes (and therefore in the plasma) allows us to average over the steady state period, increasing our signal to noise.

Without independent measures of the plasma conditions, which are still in the planning stages, we utilize our measured Hβ line shape, since it is the best characterized and most well understood line in the Balmer series. Comparison with Wiese et al [17] shows that the initial experimental design produces a plasma at slightly lower electron densities than

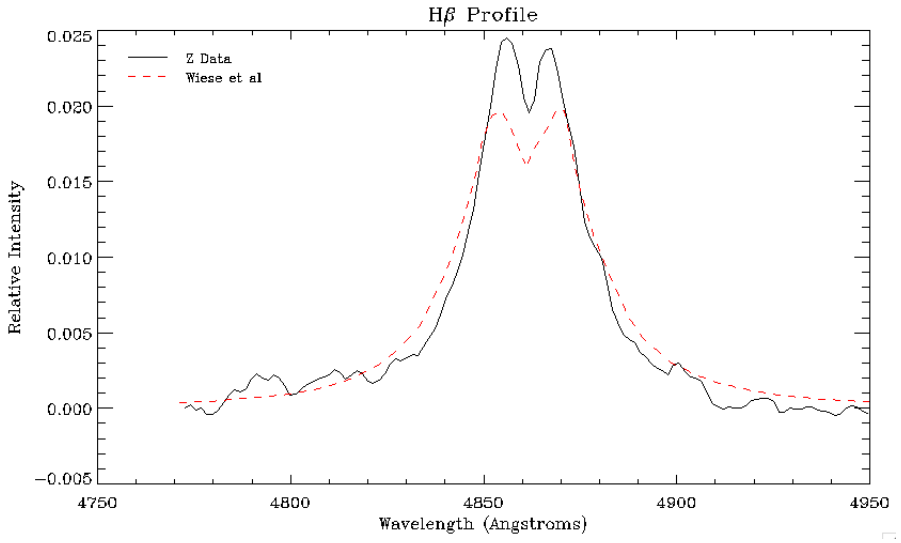

FIGURE 17. Comparison of Z data (shot z2090) to the published Hβ profile from Wiese et al.

their measurement at $8.3 \times 10^{16}\text{cm}^{-3}$ (figure 17). Fitting this same data with the VCS line broadening theory gives an electron density of 6.88×10^{16} cm^{-3}, with the assumption that Hβ is in the optically thin limit.

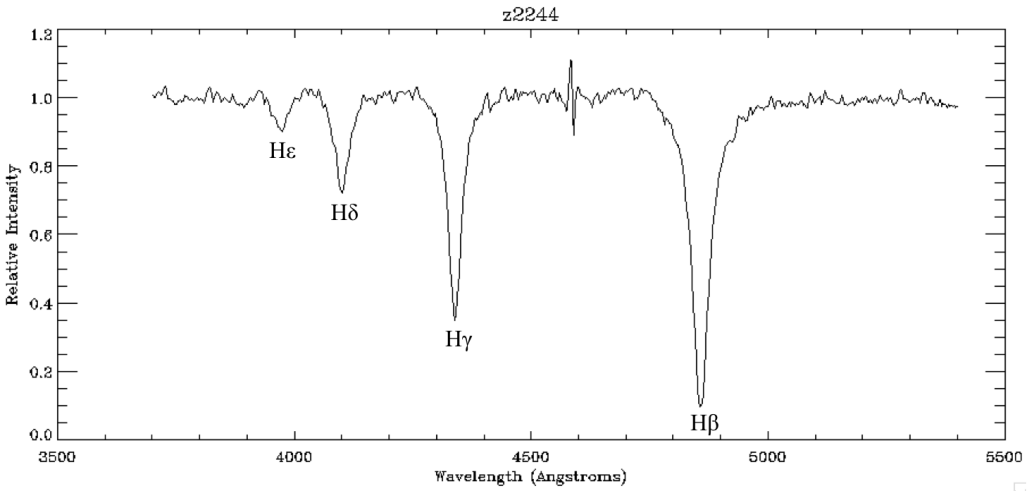

FIGURE 18. Transmission spectrum (z2244).

We obtain absorption (or transmission) spectra through two methods. In general, placing a flat piece of gold on the end of the cylinder, opposite of the fiber optic, results in absorption

measurements. Even though this piece of gold is not directly illuminated by Z-pinch radiation it is still heated by light emitted from the gold walls, to the point where it can backlight the plasma. Initially, to obtain transmission data, a null or empty shot had to be taken, in order to provide a measurement of just the radiation from the gold backlighter. Then, dividing an absorption spectrum taken with the same cell design by this null spectrum divides out the contribution from the gold, leaving only a transmission spectrum of the hydrogen in the gas cell. This method assumes, however, that each shot is identical. With the addition of a second streaked spectrometer system, and a slight cell re-design, we were able to take simultaneous spectra of the hydrogen gas and the gold backlighter. In this cell design the gold piece across from the fiber optic is tilted both 45° towards the Z-pinch so that it is also heated by the x-rays and 45° towards the vertical, where another ear and fiber optic system is located. Therefore, in addition to the original line of sight along the axis (12 cm path length), we have a perpendicular line of sight located directly above the backlighter with a path length of only 1 cm, along which the contribution from the hydrogen is negligible (except in the region of Hβ which is optically thick). Using these techniques to obtain transmission spectra gives high enough signal to noise to make the first measurements of Hϵ in these density regimes (figure 18).

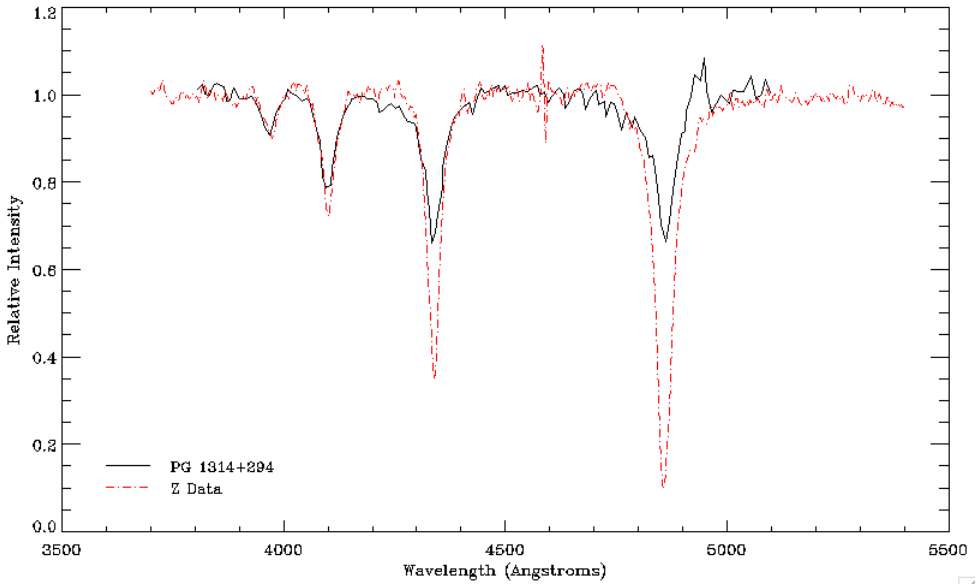

FIGURE 19. Comparison of Z data (shot z2244) with the published spectrum of a white dwarf (PG 1314+294).

Furthermore, comparison of this Z data to that of a hydrogen (DA) white dwarf star (figure 19), shows that we are indeed producing plasma conditions typical of white dwarfs, with the exception of some differences in optical depth.

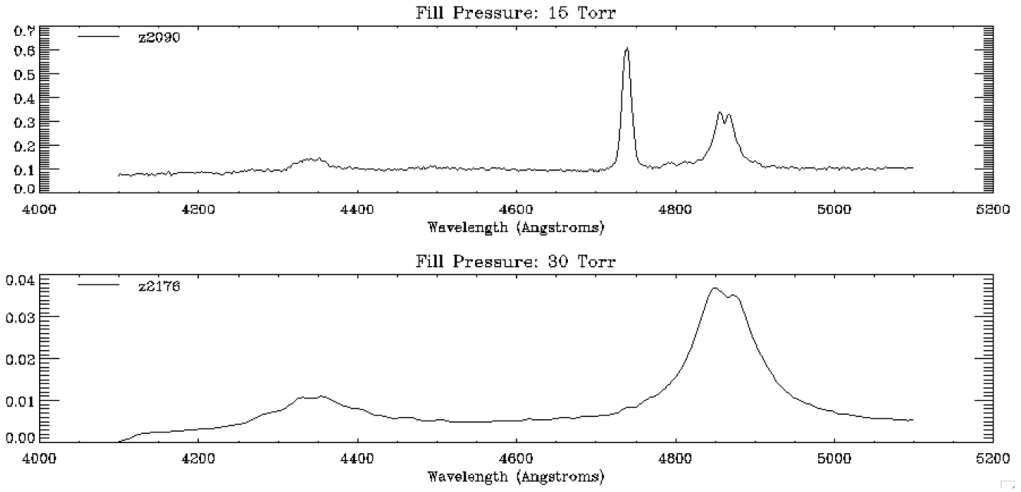

FIGURE 20. Hydrogen line profiles from shots with initial fill pressures at 15 Torr (z2090) and 30 Torr (z2176). The large spectral feature to the left of Hβ in z2090 is the comb (timing fiducial).

While it already produces the conditions achieved in previous experiments, this platform has the ability to straightforwardly be pushed to both higher and lower electron densities, primarily by adjusting the initial fill pressure of the gas cell. You can see that doubling the initial fill pressure compared to previous shots (increasing from 15 to 30 Torr) produces broader Balmer lines, corresponding to higher electron densities (figure 20). VCS fits to the Hγ line gives 6.10×10^{16} cm^{-3} for the low fill shot (z2090) and 2.57×10^{17} cm^{-3} for the high fill pressure shot (z2176), corresponding to about a factor of 4 increase in electron density. Additionally, we can also measure higher electron densities by moving the line of sight closer to the gold wall, as will be discussed later.

3.3.1. *Optical Depth.*

Optical depth, τ, is a measure of how many emitters or absorbers are along an optical path, and how strongly they emit or absorb. It is defined as $\tau = \kappa\rho x$, where κ_λ is the wavelength dependent opacity of the species in question, ρ is the density of that species, and x is the optical path length through the species. If you are looking through a gas the intensity of light absorbed is related to the optical depth by $I = I_0 e^{-\tau}$. If $\tau \gg 1$ then a spectral feature will become saturated, and wavelength dependence of the intensity can be significantly rearranged, therefore you will no longer be measuring the source function of the spectral feature, since it has been distorted by optical depth effects.

In order to measure the optical depth of our hydrogen plasma we implemented a cell design with two lines of sight, each with a different path length through the cell. This was accomplished by placing a gold plated wedge inside of the gas cell, a third of the way along

the axis. The gold wedge was tilted 45° towards the pinch on both sides, dividing the cell into two unequal parts and backlighting both of these lines of sight. The entire length of the cell is 12 cm, and it is divided into two path lengths of 3 cm and 7 cm. With this set up we can measure I_s and I_l from the short and the long path length line of sight on a single shot. Therefore,

$$\frac{I_s}{I_l} = \frac{I_0 e^{-\tau_s}}{I_0 e^{-\tau_l}} = e^{-\tau_s + \tau_l}$$

where $\tau_l = \kappa\rho x_l$ and $\tau_s = \kappa\rho x_s$. Since these measurements are made on a single shot the plasma conditions on either side of the dividing wedge should be identical, so $\kappa\rho$ should be the same for both the long and short path length. In this case the only factor contributing to the optical depth is the difference in path length so

$$\tau_l = \frac{7}{3}\tau_s$$

$$\frac{I_s}{I_l} = e^{\tau_s(7/3-1)} = e^{\frac{4}{3}\tau_s}$$

$$\tau_s = \frac{3}{4}\ln[\frac{I_s}{I_l}]$$

.

This cell design has been fielded on two different shots, allowing this analysis to be conducted twice (figure 21 and figure 22). In both shots the optical depth could only be found for Hβ and Hγ because the higher order lines are not seen in the short path length.

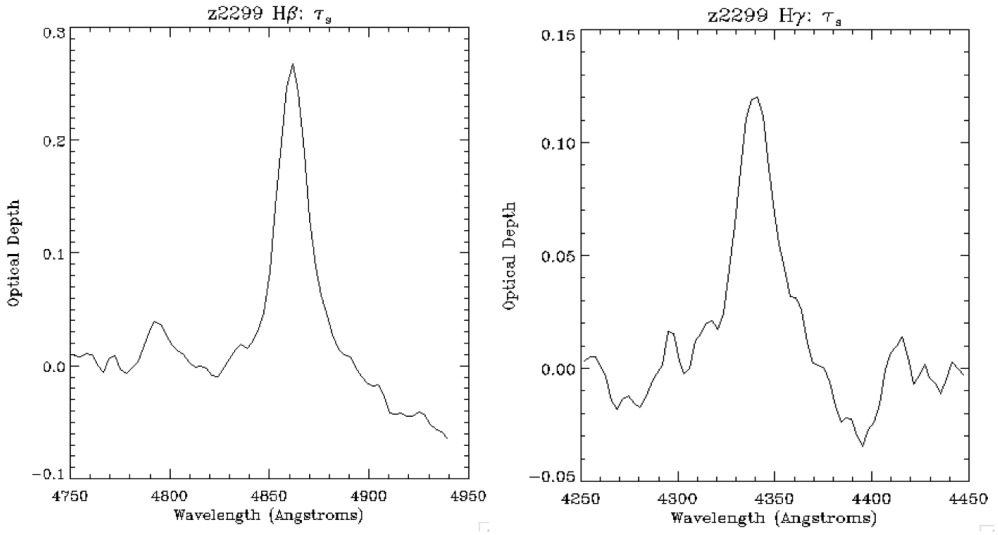

FIGURE 21. Optical depth as a function of wavelength for Hβ and Hγ for a path length of 3 cm (z2299).

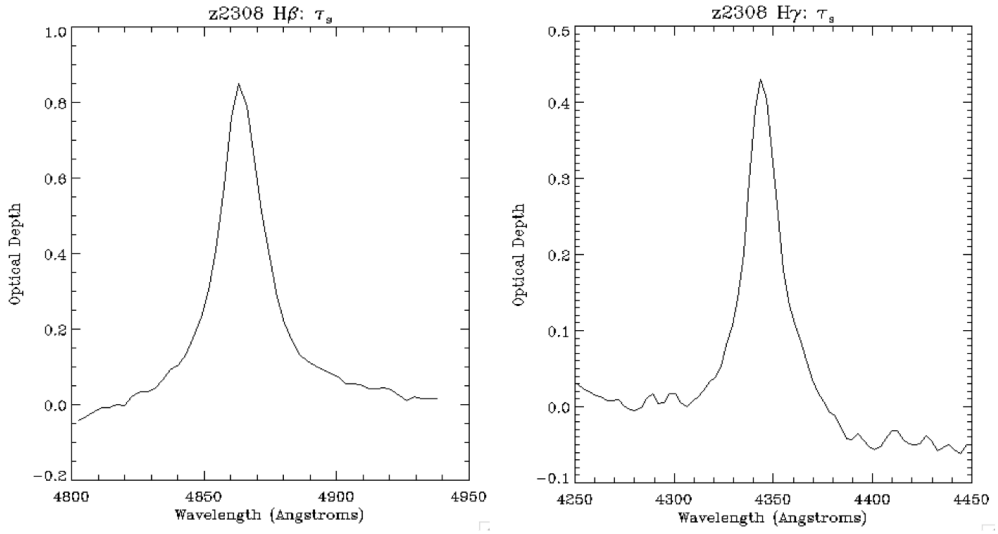

FIGURE 22. Optical depth as a function of wavelength for Hβ and Hγ for a path length of 3 cm (z2308).

It can be seen that optical depth is strongly dependent upon the plasma conditions, since the variation between these two shots resulted in a little more than a factor of three increase in τ from z2299 to z2308. However the optical depth for Hβ and Hγ scale in a similar way, since the ratio $\tau_\beta/\tau_\gamma \approx 2$ is preserved. If these two shots are typical of the scatter in optical depth from shot to shot, then for a 12 cm cell the optical depth would be 4 times the optical depths found here. Therefore $\tau_\beta \approx 1.08 - 3.28$ and $\tau_\gamma \approx 0.48 - 1.76$, so H$\beta$ is almost certainly optically thick and Hγ may suffer some optical depth effects as well.

3.3.2. *Thermodynamics of the Z driven hydrogen plasma.*

We began this experiment with the hope that the plasma would be in local thermodynamic equilibrium (LTE), which would allow for more straightforward analysis. In emission all of the spectral lines are coming from transitions from an upper level state to the n=2 state. The observed intensity of the spectral line is therefore given by $I_{2,k} \propto A_{2,k}N_k$, where $A_{2,k}$ is the Einstein A coefficient for spontaneous emission between states n=k and n=2, and N_k is the population of the upper state. With an absolute calibration it would be possible to directly determine the upper state population from absolute intensity measurements, however even without this calibration we can use relative line strengths.

In complete LTE the level populations are determined solely by collisional processes and are given by the Boltzmann distribution,

$$\frac{N_j}{N_k} = \frac{g_j}{g_k} e^{-(E_j - E_k)/T}$$

where g is the degeneracy and E is the energy of the level, and T is the temperature. However if there was a deviation from LTE due to the radiation field from the gold wall, there would be a radiative contribution to the level populations given by,

$$\frac{N_j}{N_k} = \frac{f_{2,j}}{f_{2,k}} \frac{B(\lambda_j, T)}{B(\lambda_k, T)}$$

where f is the oscillator strength for the transition between the upper state and n=2 and $B(\lambda, T)$ is the number of photons from the gold wall that can drive transitions to the upper level state which is given by a modified Planck distribution, $B(\lambda, T) = (\frac{2hc^2}{\lambda^5} \frac{1}{e^{hc/\lambda T}-1}) \frac{\lambda}{hc}$ (where the factor of $\frac{\lambda}{hc}$ converts from energy per wavelength to photon number per wavelength).

Taking the ratio of the integrated intensities of the Hβ and Hγ lines cancels out the factor of the N_2 population leaving $I_\gamma/I_\beta = (N_5/N_4)(A_{2,5}/A_{2,4})$. Therefore, for a given temperature of the gold wall and hydrogen plasma the relative contributions of radiative and collisional processes to the level populations can be determined by

$$\frac{I_\gamma}{I_\beta} \frac{A_{2,4}}{A_{2,5}} = a \frac{g_5}{g_4} e^{-(E_5 - E_4)/T} + b \frac{f_{2,5}}{f_{2,4}} \frac{B(\lambda_5, T)}{B(\lambda_4, T)}$$

where a is the amount that the level populations are driven by collisions, b is the amount that the level populations are driven by radiation from the gold, and $a + b = 1$.

Relative importance of collisional vs radiative contributions to level populations.					
Shot	I_γ/I_β	$n_e(\text{cm}^{-3})$	Saha Temp (K)	Collisional (a)	Radiative (b)
z2086	0.232	6.30×10^{17}	14,816	0.367	0.633
z2090	0.193	6.22×10^{16}	10,671	0.220	0.780
z2127	0.199	8.06×10^{16}	11,021	0.248	0.752

This does assume both a temperature for the gold and a temperature for the hydrogen plasma. However, in this case the ratio of blackbody photons driving transitions from n=2 to n=4 to photons driving transitions from n=2 to n=5 is an insensitive function of temperature, as this is in the Rayleigh-Jeans tail for a gold temperature in the region of $\approx$ 5eV. The hydrogen gas temperature, on the other hand, appears in the collisional term, and if the plasma were in LTE the ionization fraction would be governed by the Saha equation, $\frac{n_{i+1} n_e}{n_i} = \frac{Z_{i+1} g_e}{Z_i} \frac{(2\pi m_e kT)^{3/2}}{h^3} e^{-\frac{\chi_i}{kT}}$ where n is the number density, Z is the partition function, and χ is the ionization energy. The Saha equation can then be used to find an LTE temperature given an ionization fraction, which is the ratio of the initial number density (from the fill pressure) to the electron density obtained through VCS fits.

Another consideration is that Hβ is likely optically thick, which decreases the measured line intensity. Therefore the inherent Hβ/Hγ intensity ratio is actually larger than measured, which will result in a slight decrease in the radiative contribution. However, from this analysis it can still be seen that the dominant contribution to the level populations in our plasma is radiative, and therefore the assumptions of LTE cannot be applied to our experiment.

3.3.3. *Heating Mechanism.*

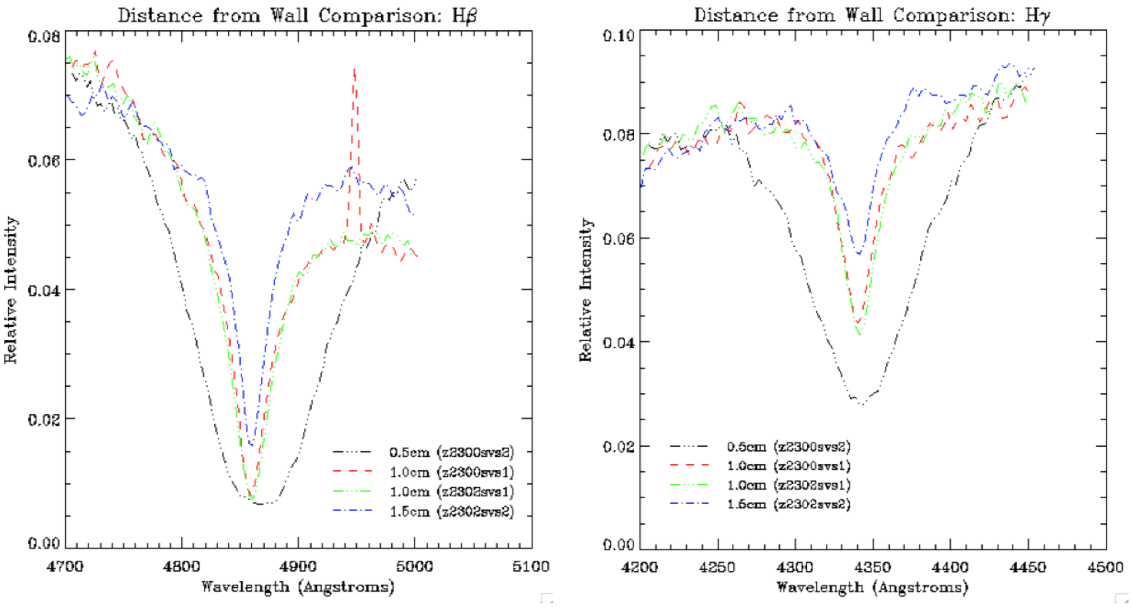

FIGURE 23. Variation in Hβ and Hγ profiles with distance from the gold wall. The emission looking feature on the red shoulder of Hβ in z2300svs1 (red) is an artifact on the film.

In order to verify the picture that it is re-radiation from the gold that is heating the hydrogen we introduced a new cell design with adjacent axial lines of sight at different distances from the gold wall. In the case of a cylindrical gas cell there is a line of sight at the normal distance (directly on axis) at 1.0 cm from the back wall, and another line of sight located at 0.5 cm from the back wall. Additionally, we fielded a rectangular cell, allowing for three lines of sight at 0.5 cm, 1.0 cm, and 1.5 cm from the back wall. For both the rectangular and cylindrical cell design there was a piece of gold opposite the fiber input, tilted 45° towards the Z-pinch in order to serve as a backlight, and no vertical line of sight.

It is demonstrated qualitatively from the width of the lines (figure 23) that the electron density, and therefore ionization, is significantly higher at the 0.5 cm away line of sight and falls off with increasing distance from the gold wall. This confirms the idea that it is radiation from the gold that is heating and photoionizing our hydrogen plasma, and not the initial x-rays or some other mechanism. Furthermore, these line shapes give more evidence that Hβ is optically thick, because the depth of the absorption lines hardly change for Hβ while they decrease substantially for the Hγ line.

In a more quantitative analysis we fit the VCS theory to small lineouts in time (10-20ns depending on signal strength); the Hγ line was chosen because Hβ is optically thick and

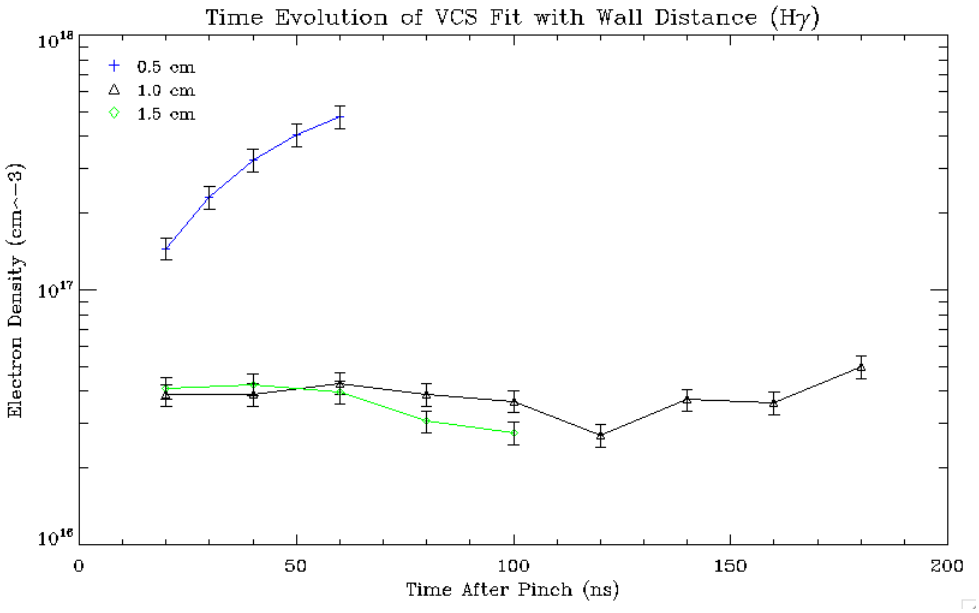

FIGURE 24. Results of VCS fit to sequential lineouts at different distances from the back wall.

Hδ is much fainter. This shows that the electron densities in the 0.5 cm line of sight are an order of magnitude higher than those farther away from the wall, and continuously increasing (figure 24). There also appears to be almost no difference in the ionization levels at the 1.0 and 1.5 cm lines of sight, indicating that we are not only looking at a steady state region in time, but that the plasma is also fairly spatially uniform once you back away from the wall. Since our measurement inevitably averages over some finite spatial extent (the beam width within the cell) this spatial uniformity is convenient.

3.3.4. *Swan Bands.*

An unexpected advantage of the two previously mentioned gas cells, designed for opacity or heating measurements, was the measurement of the Swan bands. These are prominent carbon features that are seen in carbon atmosphere (DQ) white dwarfs, as well as other stars. They are named for William Swan, who first studied the spectrum of C_2. We had not anticipated this, but since the gold back lighter wedges are only tilted 45° towards the pinch (without an additional 45° tilt towards a vertical line of sight) direct reflections of light transmitted through the Mylar makes it into our detector. Though the z-pinch power distribution is heavily concentrated in x-rays, there are some visible photons that we can detect at the same time as those x-rays are interacting with the Mylar window. Looking at the streak data (figure 25) you can see three distinct regions before the onset of radiation from the gold and hydrogen absorption. There is an initial period where there appears to be little to no spectral signals, which is expected because initially Mylar is transparent

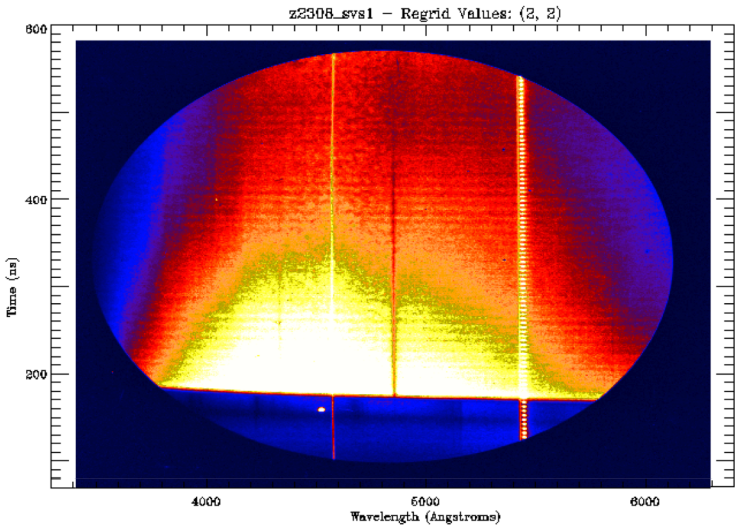

FIGURE 25. Streaked data from z2308, clearly showing the Swan bands in absorption before the onset of radiation from the gold.

to visible photons. Then there is a phase where there is nearly uniform absorption across wavelengths, and then finally the Swan bands are seen.

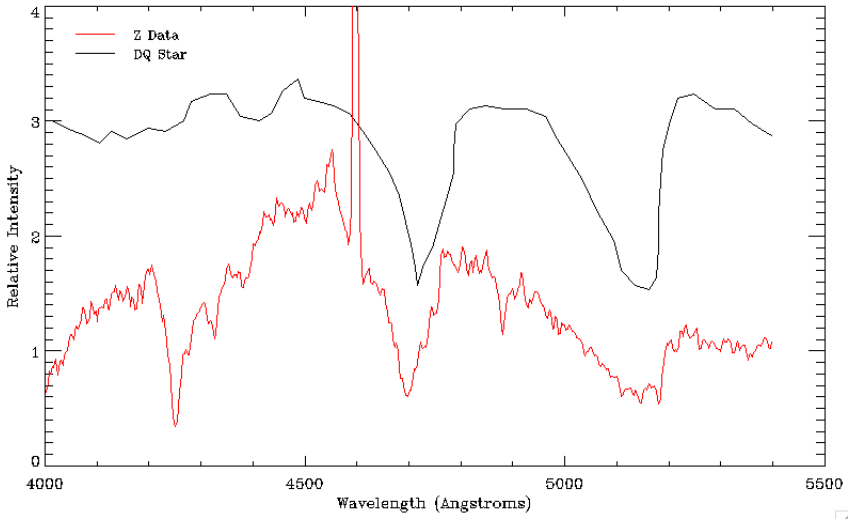

FIGURE 26. Comparison of a DQ white dwarf (SDSS J1356-0009) with data from the Z experiments. Data is scaled and vertically displaced.

Comparing the spectrum in this latter time to that of a DQ white dwarf star (figure 26) shows that these features are quite similar in both the white dwarf and our data from Z. We may be able to exploit this similarity to give us clues about the plasma conditions in the atmospheres of cool DQ white dwarfs.

4. Results

4.1. **Comparison of Line Broadening Theories.**

We have compared the Hβ, Hγ, and Hδ line profiles from Tremblay and Bergeron (TB) [20] across a grid of temperatures and electron densities with the profiles predicted by both Vidal-Cooper-Smith (VCS) [21] and Kepple-Griem (KG) [22]. Because our plasma is not in LTE electron density and temperature are decoupled, and can be treated independently. In this case the temperature dependence of the line shape is much smaller than the dependence upon electron density (Appendix I). Therefore, I will only be discussing the variation with electron density, at a fixed temperature of 10,000K. In order to quantitatively compare these different line broadening theories we fit profiles from TB and KG with the VCS theory, obtaining the VCS opinion of the electron density. If the two theories were in agreement the VCS fit would recover the input electron density for the other profile, and plotting the input electron density against the electron density found by VCS would yield a diagonal line (figure 27, figure 28). However, the fits diverge from this line. KG and VCS show substantial differences across all electron densities, and the variations between TB and VCS increase with the order of the line and with increasing electron density (Appendix I, figure 27).

From this comparison we can see that in order to provide data to successfully test the differences between these line broadening theories this experiment must explore the higher density ($N_e > 3 \times 10^{16}$ cm^{-3}) regimes and measure the higher order lines.

4.2. **Comparison of Z Data with Theory.**

From the above analysis we concluded that in order to best test the line broadening theories in question we must either push to higher electron densities or higher order lines.

4.2.1. *Higher Order Lines.*

We have successfully measured Balmer lines up to Hϵ. We do not currently have access to a spectrally independent measure of our plasma conditions, so we cannot compare our data to line broadening theories in an absolute sense. However, we can investigate the internal consistency, by finding the VCS opinion of the electron density for multiple hydrogen lines measured on the same shot, and therefore at the same plasma conditions.

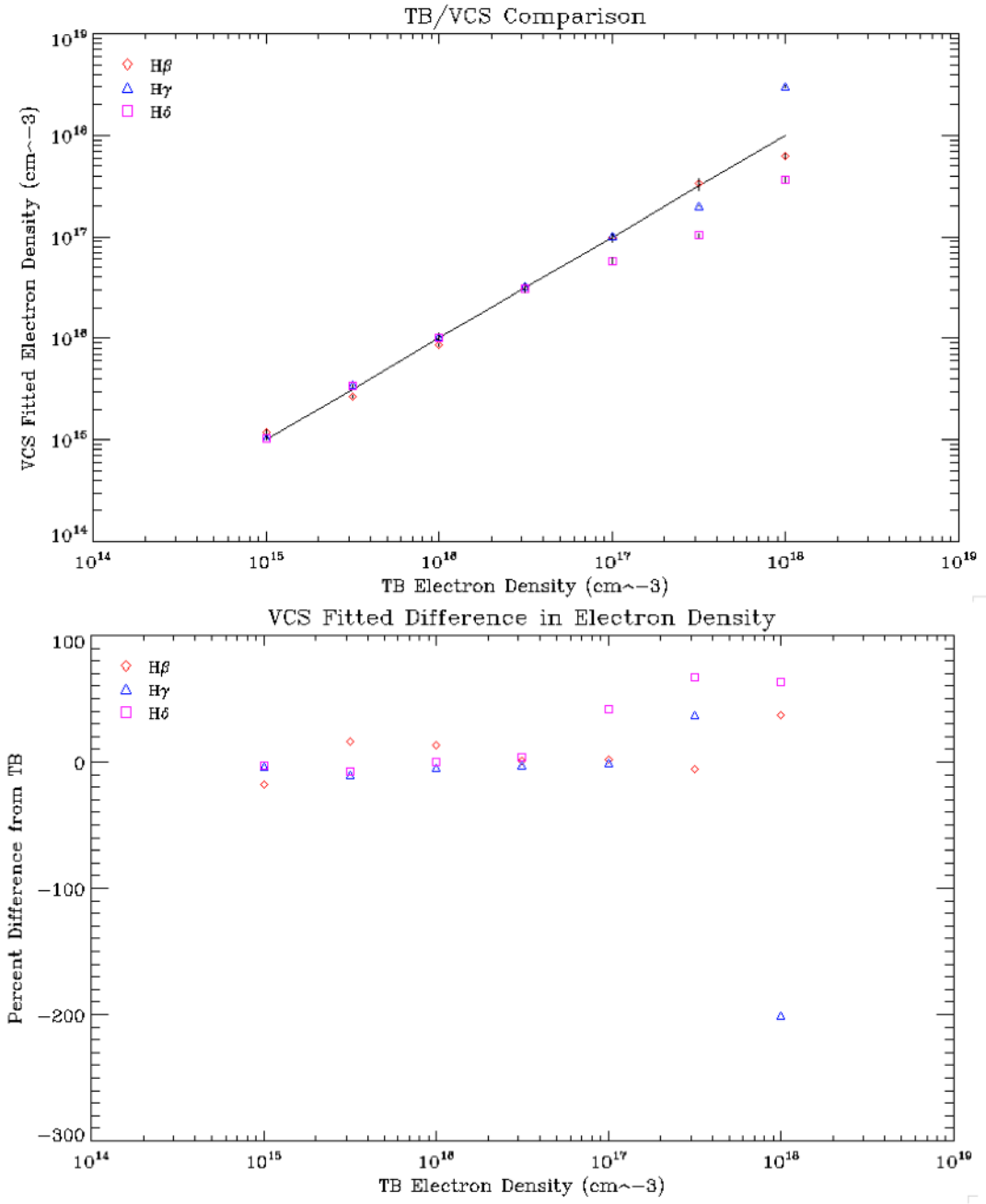

FIGURE 27. VCS fit of TB profiles. The largest differences occur at higher electron densities, and for the higher order lines in the Balmer series.

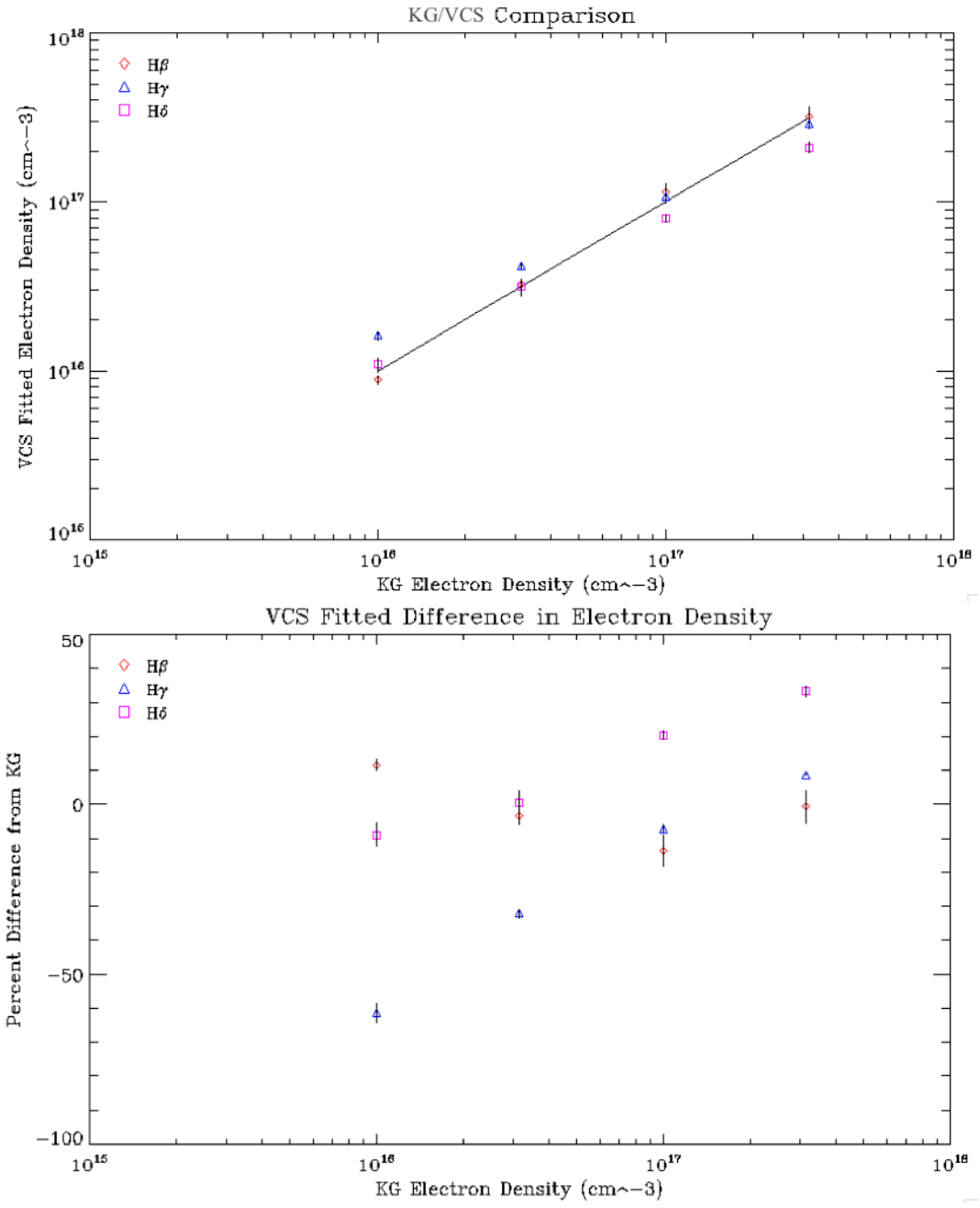

FIGURE 28. VCS fit of KG profiles. There are similarly large differences for all electron densities considered.

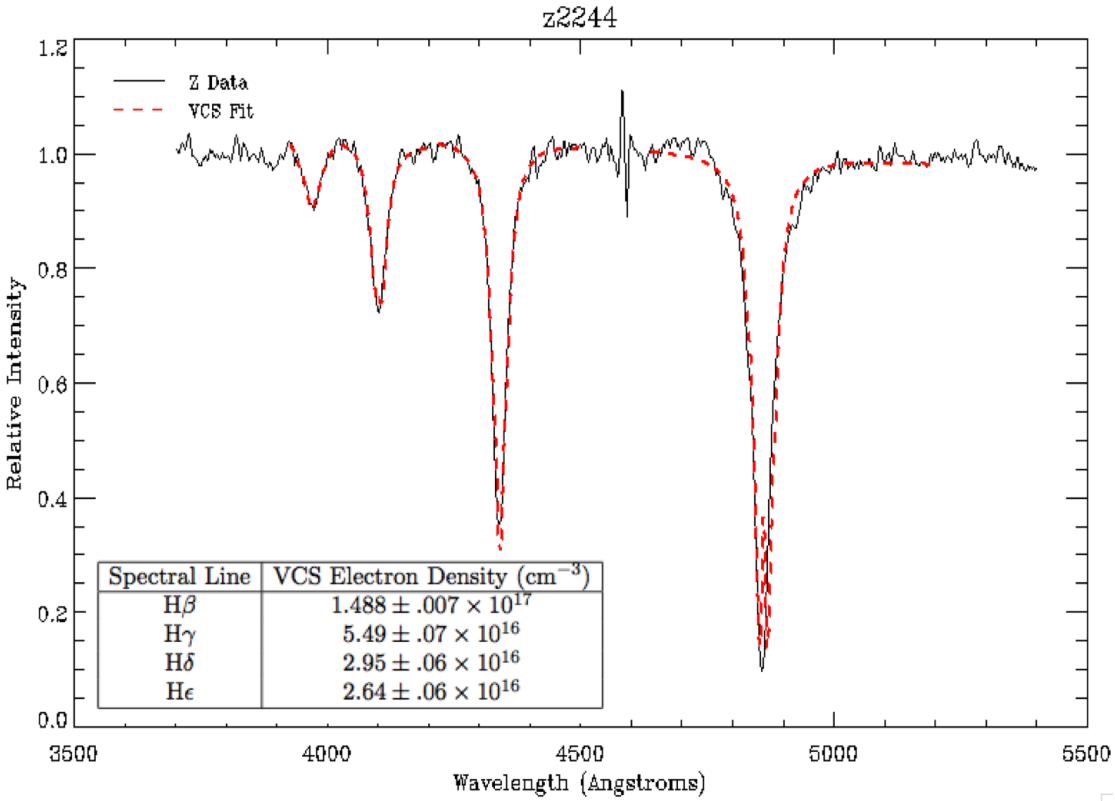

FIGURE 29.

You can see that the VCS profiles are able to reproduce our Z profiles, for all of the measured lines ($H\beta - H\epsilon$), however the electron densities that it returns for each spectral line are not identical (figure 29). We expect $H\beta$ to be optically thick, and therefore it is not a surprise that the electron density found by VCS is higher for $H\beta$ than for the other Balmer lines. The electron densities obtained by VCS for $H\delta$ and $H\epsilon$, however, agree to within 2.85%. Therefore the discrepancy in the electron density found from $H\gamma$ may be an indicator that this spectral line is suffering from optical depth effects as well.

4.2.2. *Higher Electron Densities.*

The highest electron densities that we have achieved in our experiment so far are at the 0.5 cm from the wall line of sight in the cell's designed to verify the picture that re-radiation from the gold is driving our hydrogen plasma. As discussed above, in this case the plasma never reaches any kind of steady state. Instead the electron density continues to increase until the spectral lines are broadened completely into the continuum (figure 30). This allows us to test line broadening theories at the extreme high density limit. Furthermore, this provides us with an additional tool: the Inglis-Teller limit [23].

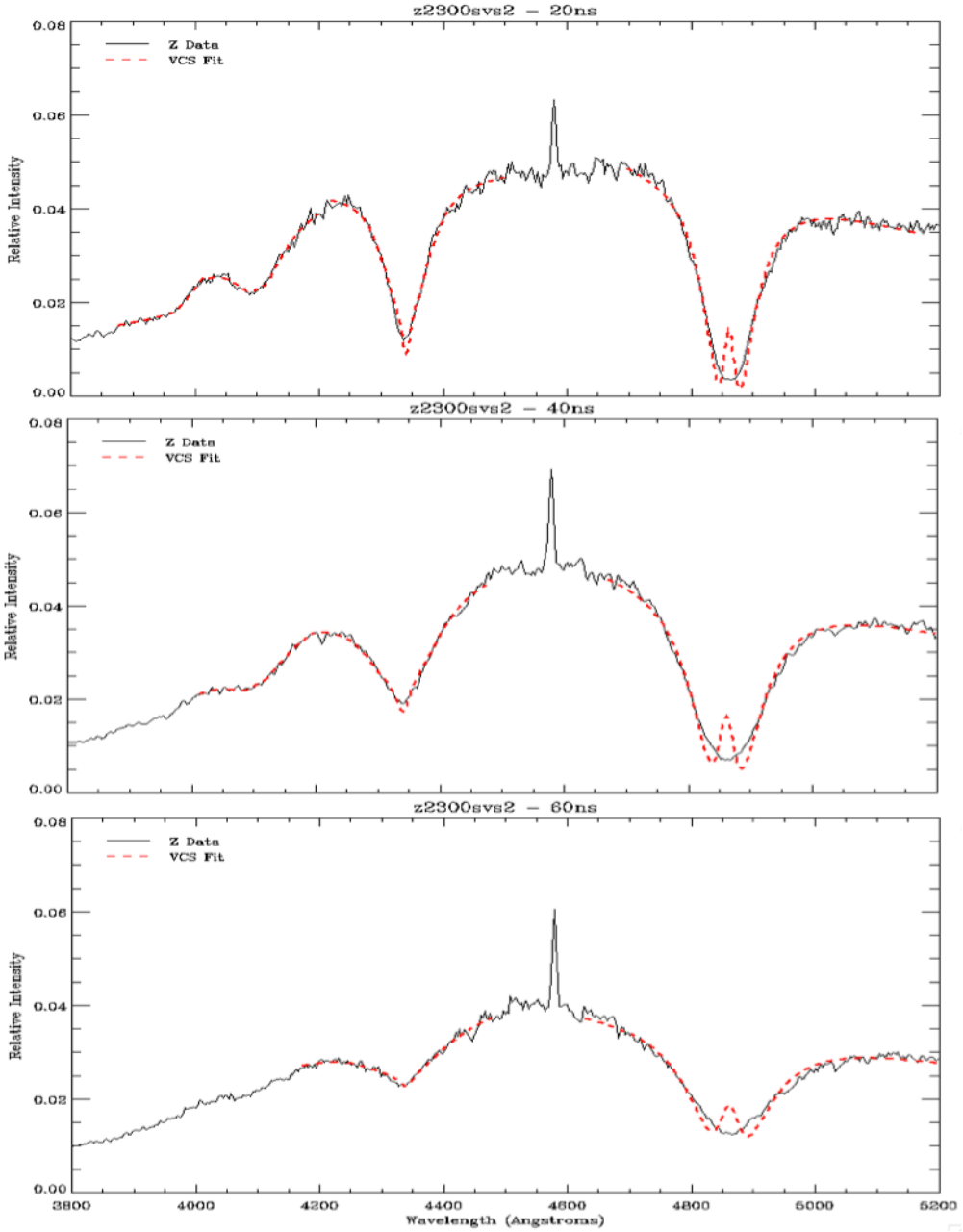

FIGURE 30. z2300svs2 - 20ns wide lineouts at different times after the pinch. Hβ, Hγ, Hδ, and Hϵ are initially visible, then Hϵ and then Hδ are broadened out.

The Inglis-Teller limit describes at what electron and ion density a given line will become Stark broadened into the continuum. For the Balmer series it is given by

$$Log[N_e + N_i] = 23.491 - 7.5Log[n_{max}]$$

where N_e and N_i are the electron and ion number densities in cm^{-3} and n_{max} is the upper quantum number of the last observable spectral line. Since our plasma is pure hydrogen $N_e = N_i$. This relation can be used to place a limit on electron density depending on which spectral lines can be seen. In doing so we can check the internal consistency of the VCS fits, and the consistency of the VCS fits with the Inglis-Teller limit.

Electron densities (cm^{-3}) implied by the Inglis-Teller limit and VCS fits to the observable spectral lines.					
Time (ns)	n_{max}	Inglis-Teller	Hϵ	Hδ	Hγ
20	7	7.11×10^{16}	$(2.24 \pm .04) \times 10^{17}$	$(9.8 \pm .3) \times 10^{16}$	$(1.467 \pm .005) \times 10^{17}$
40	6	2.26×10^{17}		$(1.05 \pm .01) \times 10^{17}$	$(2.58 \pm .4) \times 10^{18}$
60	5	8.87×10^{17}			$(3.23 \pm .3) \times 10^{17}$

You can see that for the higher electron densities the line profile fits are inconsistent, with each other, and with the Inglis-Teller limit. At the 20ns time step the highest order line that can be seen is Hϵ so the Inglis-Teller limit places the electron density between 7.11×10^{16} and 2.26×10^{17} cm^{-3}, and all of the VCS fit electron densities do fall in this range. However, there is a 40% scatter between the different lines. The agreement with the Inglis-Teller limit stops there though, and looking at the Hγ line, the electron density jumps around wildly by an order of magnitude. In these regimes the hydrogen lines are far from isolated, as they have begun to completely blend together and into the continuum, and you can see that we are really pushing the line broadening theory farther than it can go.

5. Conclusions

Using the x-ray flux produced by the Z Pulsed Power Facility at Sandia National Laboratories we produce a stable hydrogen plasma at white dwarf photospheric conditions. We measure time resolved hydrogen spectra at electron densities that are tunable over at least an order of magnitude. We have demonstrated that the hydrogen plasma is photo-pumped by radiation from the gold walls of the gas cell, after that gold absorbs and is heated by the initial x-ray pulse from the z-pinch. We have also established that, while the higher order lines are in the optically thin limit, the Hβ line is optically thick and the Hγ line shape may show some optical depth effects as well. Comparison of three different line broadening theories shows $\approx 10 - 20\%$ differences, even between Hβ line profiles at relatively low electron densities. These differences increase both with electron density and with the order of the spectral line. However at some point the higher order lines do become broadened into the continuum and may not be observable at these very high electron densities (greater than a few times 10^{17} cm^{-3}). Comparison with our Z data shows that VCS can reproduce

our measured profiles, but the electron densities returned in the high electron density limit are not consistent between lines or with the Inglis-Teller limit.

6. Future Plans

In general the planned future developments of this project can be broken down into two categories: the scientific goals and the experimental challenges that must be overcome to achieve them. The main science driver for this project is to provide measurements with which to test hydrogen line broadening theories, with the ultimate goal of improving white dwarf atmospheric models. This platform has a potential well beyond this. Once it is fully developed it will be able to be easily be modified to accommodate different different gas fills relevant to white dwarfs, such as helium or carbon. Additionally, it could presumably be applied to different astrophysically relevant temperature and density regimes, such as those in gas giant planets.

While we have made steps towards the understanding and development of this experimental platform, there is still more to be done. There is a new cell design, that we will be fielding on the next shot series, that allows simultaneous measurements of emission and absorption through the same plasma (figure 31). This will allow us to draw definitive conclusions about the level populations since we will be able to see all of the states at once. We are also working towards absolute spectral intensity calibrations and a bolometry diagnostic, which will utilize absolute calibrations to infer the temperature of the gold walls. The ultimate experimental goal, however, is to obtain spectrally independent measures of the plasma conditions. The prime candidate for this is optical Thompson scattering, and such a diagnostic is being developed for the Z platform, but it is still far from implementation.

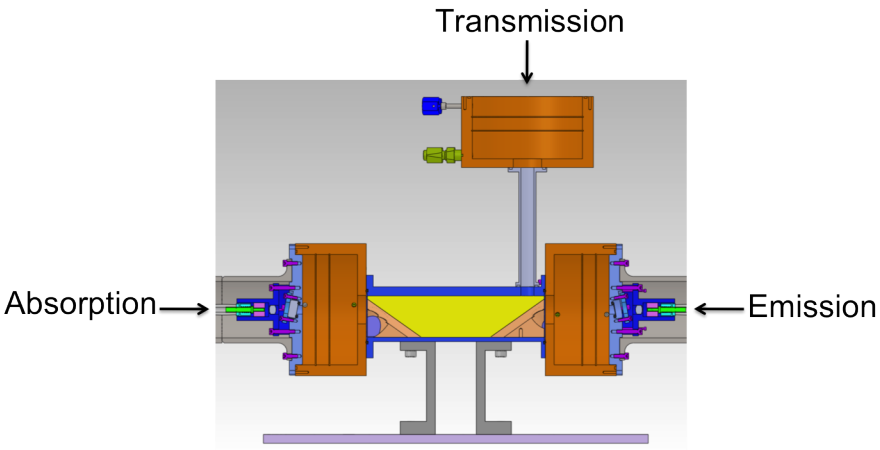

Figure 31. New cell design, providing simultaneous measurement of emission, absorption, and transmission spectra.

This project is very exciting, in that it is ushering in a new era of laboratory astrophysics. Experimental capabilities have only recently progressed to the level where high energy density facilities, like the Z-Machine, can create macroscopic chunks of material at astrophysically relevant conditions. Bringing astrophysical problems into the laboratory, where conditions can be manipulated and directly controlled, will provide a valuable complement to aid in our understanding and interpretation of astrophysical observations.

7. Acknowledgements

This research would not be possible without the wonderful team of people involved in this collaboration, both at UT Austin and Sandia National Laboratories. On the Sandia side, the experimental guidance and operational experience offered by Dr. Gregory Rochau and Dr. Jim Bailey are invaluable. Alan Carlson and Dr. Matthew Gomez have been our leading resources in the development of the streaked spectrometer system. Back at UT, this project is conducted under the guidance of Dr. Don Winget and Dr. Mike Montgomery, with graduate students Ross Falcon and Thomas Gomez, and undergraduate Travis Pille. Additionally, his experience and insight makes the guidance of Dr. Roger Bengtson invaluable as well. I would like to thank Dr. Winget and Dr. Bengtson for the opportunity and privilege to work with them. I would also like to thank Dr. Montgomery, and all of the aforementioned, for the many stimulating conversations and for everything I've learned from them.

References

[1] D. E. Winget, adapted from StarDate Magazine.
[2] S. O. Kepler et al, *White dwarf mass distribution in the SDSS*, Monthly Notices of the Royal Astronomical Society, **375**, 1315 (2007)
[3] Ross E. Falcon, D. E. Winget, M. H. Montgomery, and Kurtis A. Williams, *A Gravitational Redshift Determination of the Mean Mass of White Dwarfs. DA Stars*, Astrophysical Journal, **712**, 585 (2010)
[4] Ross E. Falcon, private communication.
[5] David J. Griffiths, *Introduction to Quantum Mechanics*, Pearson Prentice Hall (New Jersey), 2005.
[6] Richard H. Leonard and Stanley L. Huddelstone, *Plasma Diagnostic Techniques*: Chapter 6, Academic Press, 1965.
[7] Roger D. Bengtson, J. D. Tannich, and P. Kepple, *Comparison Between Measured and Theoretical Stark-Broadened Profiles of $H_6 - H_{12}$ Emitted from a Low-Density Plasma*, Phys. Rev. A, **1**, 532 (1970)
[8] Roger D. Bengtson and Gerald R. Chester, *Stark broadening of Balmer lines in the density range $(2-8) \times 10^{14} cm^{-3}$*, Phys. Rev. A, **13**, 1762 (1976)
[9] D. L. Evans, D. P. Aeschliman, and R. A. Hill, *Comparison of H_β theory and experiment at electron densities near $10^{15} cm^{-3}$*, Phys. Rev. A, **10**, 2430 (1974)
[10] E. A. McLean and S. A. Ramsden, *Optical Interferometric and Spectroscopic Measurements of Electron Density in a Plasma*, Phys. Rev., **140**, 1122 (1965)
[11] J. C. Morris and R. U. Krey, *Experimental Test of H_β Stark-Broadening Theory at High Electron Densities*, Phys. Rev. Lett., **21**, 1043 (1968)
[12] J. B. Shumaker, Jr. and C. H. Popenoe, *Experimental Test of H_β Stark-Broadening Theory at High Electron Densities*, Phys. Rev. Lett., **21**, 1046 (1968)

[13] D. E. Kelleher and W. L. Wiese, *Observation of Ion Motion in Hydrogen Stark Profiles*, Phys. Rev. Lett., **31**, 1431 (1973)
[14] W. L. Wiese, D. E. Kelleher, and V. Helbig, *Variations in Balmer-line Stark profiles with atom-ion reduced mass*, Phys. Rev. A, **11**, 1854 (1975)
[15] Hans R. Griem, *Spectral Line Broadening by Plasmas*, Academic Press, Inc. (London), 1974.
[16] R. A. Hill and J. B. Gerardo, *Stark Broadening of H_β, H_γ, and H_δ: An Experimental Study*, Phys. Rev., **162**, 45 (1967)
[17] W. L. Wiese, D. E. Kelleher, and D. R. Paquette, *Detailed Study of the Stark Broadening of Balmer Lines in a High-Density Plasma*, Phys. Rev. A, **6**, 1132 (1972)
[18] Roger D. Bengtson et al, *Measurements of the Stark Broadening of $H\gamma$*, The Astrophysical Journal, **157**, 957 (1969)
[19] Adapted from Hamamatsu, *Guide to Streak Cameras*, http://sales.hamamatsu.com/assets/pdf/catsandguides/e_streakh.pdf
[20] P.-E. Tremblay and P. Bergeron, *Spectroscopic Analysis of DA White Dwarfs: Stark Broadening of Hydrogen Lines Including Nonideal Effects*, The Astrophysical Journal, **696**, 1755 (2009)
[21] C. R. Vidal, J. Cooper, and E. W. Smith, *Hydrogen Stark-Broadening Tables*, The Astrophysical Journal Supplement Series, **25**, 37 (1973)
[22] P. Kepple and Hans R. Griem, *Improved Stark Profile Calculations for the Hydrogen Lines $H\alpha$, $H\beta$, $H\gamma$, and $H\delta$*, Physical Review, **173**, 317 (1968)
[23] Y. P. Varshni, *Electron density in the emission-line region of Wolf-Rayet stars*, Astrophysics and Space Science, **56**, 385 (1978)

8. Appendix I - Balmer line profiles.

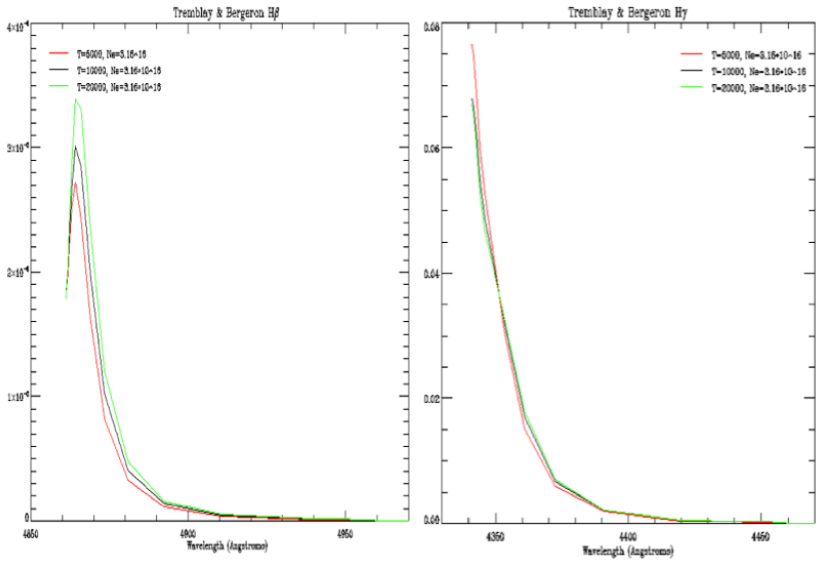

Figure 32. TB profiles at three different temperatures, and a fixed electron density for the Hβ and Hγ lines.

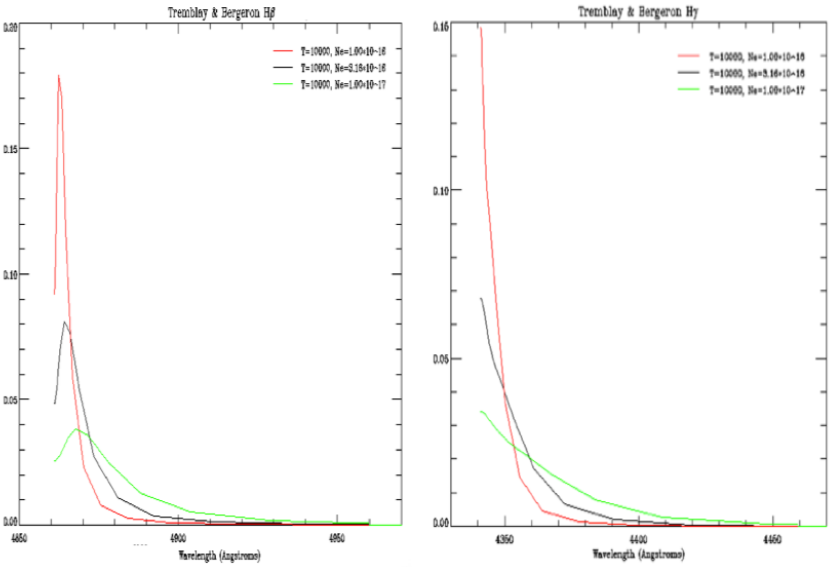

Figure 33. TB profiles at three different electron densities, and a fixed temperature for the Hβ and Hγ lines.

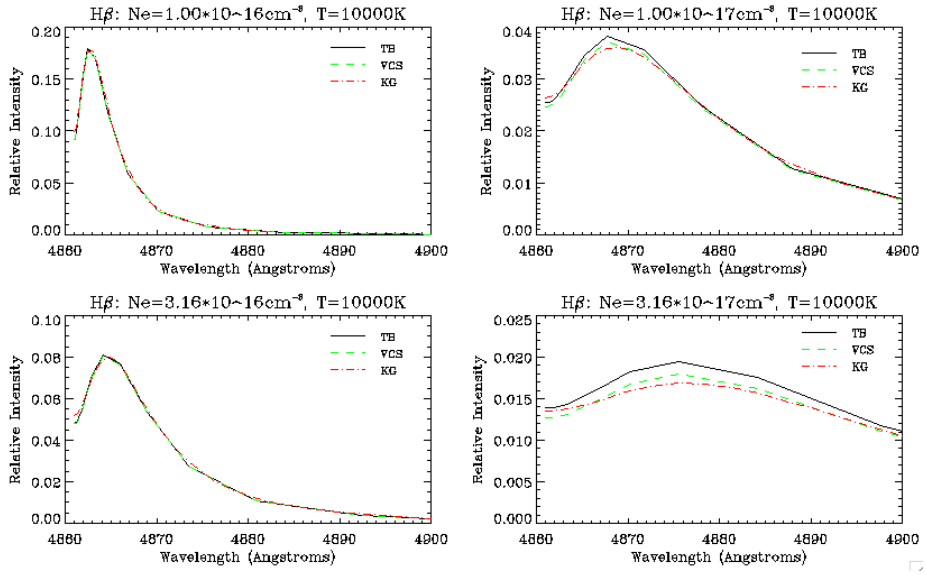

FIGURE 34. Theoretical H_β line shapes of Vidal-Cooper-Smith (VCS), Kepple-Griem (KG), and Tremblay-Bergeron (TB) at 10,000K and a grid of electron densities.

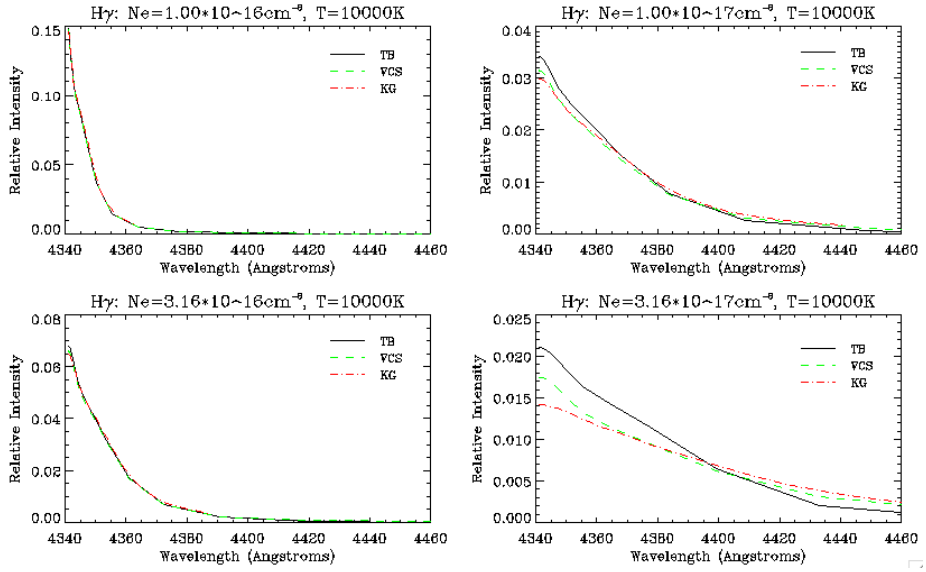

FIGURE 35. Theoretical H_γ line shapes of Vidal-Cooper-Smith (VCS), Kepple-Griem (KG), and Tremblay-Bergeron (TB) at 10,000K and a grid of electron densities.

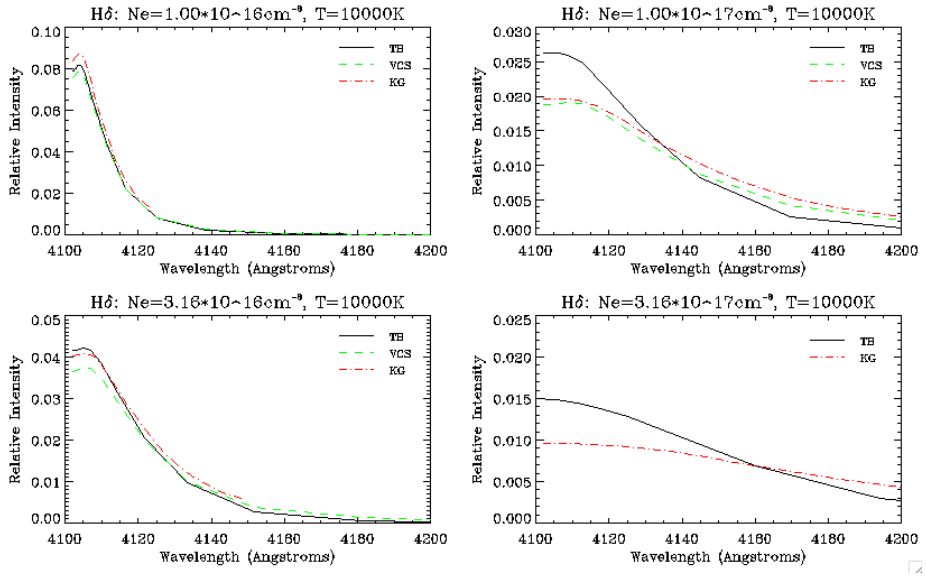

FIGURE 36. Theoretical H_δ line shapes of Vidal-Cooper-Smith (VCS), Kepple-Griem (KG), and Tremblay-Bergeron (TB) at 10,000K and a grid of electron densities.

9. Appendix II - Shot Archive

Shot Number		Comments
z2084	Absorption	Faint
z2085	Null Shot	
z2086	Emission	
z2090	Emission	
z2091	Absorption	
z2127	Emission	
z2128	Emission	Contaminates
z2129	Emission	Contaminates
z2153	Emission	Helium
z2154	Emission	Helium
z2155	Emission	Helium
z2175	Emission	Faint
z2176	Emission	
z2218	Emission	Contaminates
z2219	Emission	Contaminates
z2220	Null Shot	
z2221	Emission	Contaminates, Streak camera problems
z2222	Emission	Contaminates, Streak camera problems
z2242	Absorption	
z2243	Null Shot	
z2244	Absorption	
z2267	Absorption	2 streaks, 12cm&1cm path lengths
z2268	Null Shot	2 streaks, 12cm&1cm path lengths
z2269	Absorption	2 streaks, 12cm&1cm path lengths
z2270	Null Shot	2 streaks, 12cm&1cm path lengths
z2298	Absorption	2 streaks, rectangular cell, distance from wall, no comb, 1 streak failure
z2299	Absorption	2 streaks, rectangular cell, optical depth vs length
z2300	Absorption	2 streaks, rectangular, distance from wall
z2301	Absorption	2 streaks, rectangular cell, optical depth vs length, 1 streak failure
z2302	Absorption	2 streaks, rectangular cell, distance from wall
z2308	Absorption	2 streaks, optical depth vs length
z2309	Absorption	2 streaks, distance from wall
z2310	Absorption	2 streaks, distance from wall, contaminates

Steady State VCS Fits				
Shot	Electron Density (cm^{-3})			
	Hβ	Hγ	Hδ	Hϵ
z2086	$(5.36 \pm .02) \times 10^{16}$	$(6.89 \pm .07) \times 10^{16}$		
z2090	$(6.55 \pm .09) \times 10^{16}$	$(6.10 \pm .05) \times 10^{16}$		
z2091	$(1.74 \pm .03) \times 10^{16}$	$(1.02 \pm .01) \times 10^{16}$		
z2127	$(9.7 \pm .1) \times 10^{16}$	$(7.81 \pm .09) \times 10^{16}$		
z2176	$(3.79 \pm .07) \times 10^{17}$	$(2.57 \pm .01) \times 10^{17}$		
z2242	$(4.3 \pm .1) \times 10^{17}$	$(2.73 \pm .05) \times 10^{17}$		
z2244	$(1.488 \pm .007) \times 10^{17}$	$(5.49 \pm .07) \times 10^{16}$	$(2.95 \pm .07) \times 10^{16}$	$(2.64 \pm .06) \times 10^{16}$
z2267	$(1.19 \pm .03) \times 10^{17}$	$(6.8 \pm .2) \times 10^{16}$	$(2.53 \pm .07) \times 10^{16}$	
z2269	$(4.11 \pm .06) \times 10^{16}$	$(1.852 \pm .009) \times 10^{16}$	$(1.322 \pm .005) \times 10^{16}$	
z2299svs1	$(6.8 \pm .1) \times 10^{16}$	$(4.08 \pm .09) \times 10^{16}$		
z2299svs2	$(2.26 \pm .02) \times 10^{16}$	$(2.56 \pm .02) \times 10^{16}$		
z2300svs1	$(4.04 \pm .04) \times 10^{16}$	$(2.11 \pm .03) \times 10^{16}$	$(1.008 \pm .005) \times 10^{16}$	
z2301svs2	$(4.03 \pm .05) \times 10^{16}$	$(3.37 \pm .01) \times 10^{16}$		
z2302svs1	$(1.371 \pm .008) \times 10^{17}$	$(4.61 \pm .02) \times 10^{16}$	$(2.58 \pm .06) \times 10^{16}$	
z2302svs2	$(2.63 \pm .03) \times 10^{16}$	$(3.40 \pm .02) \times 10^{16}$		
z2308svs1	$(3.27 \pm .03) \times 10^{16}$	$(1.71 \pm .04) \times 10^{16}$		
z2308svs2	$(6.58 \pm .09) \times 10^{16}$	$(3.41 \pm .02) \times 10^{16}$	$(1.48 \pm .01) \times 10^{16}$	
z2309svs1	$(1.13 \pm .02) \times 10^{17}$	$(3.69 \pm .02) \times 10^{16}$	$(3.45 \pm .09) \times 10^{16}$	$(2.783 \pm .006) \times 10^{16}$